

# Estimates of Lightning NO<sub>x</sub> Production based on High Resolution OMI NO<sub>2</sub> Retrievals over the Continental US

Xin Zhang<sup>1,2</sup>, Yan Yin<sup>1,2</sup>, Ronald van der A<sup>2,3</sup>, Jeff L. Lapierre<sup>4</sup>, Qian Chen<sup>1,2</sup>, Xiang Kuang<sup>1,2</sup>,  
Shuqi Yan<sup>2</sup>, Jinghua Chen<sup>1,2</sup>, Chuan He<sup>1,2</sup>, and Rulin Shi<sup>1,2</sup>

<sup>1</sup> Collaborative Innovation Center on Forecast and Evaluation of Meteorological Disasters/Key Laboratory for Aerosol-Cloud-Precipitation of China Meteorological Administration, Nanjing University of Information Science and Technology (NUIST), Nanjing 210044, China

<sup>2</sup> Department of Atmospheric Physics, Nanjing University of Information Science and Technology (NUIST), Nanjing 210044, China

<sup>3</sup> Royal Netherlands Meteorological Institute (KNMI), Department of Satellite Observations, De Bilt, the Netherlands

<sup>4</sup> Earth Networks, Germantown, Maryland, USA

**Correspondence:** Yan Yin (yinyan@nuist.edu.cn)

**Abstract.** Lightning serves as the dominant source of nitrogen oxides (NO<sub>x</sub> = NO + NO<sub>2</sub>) in the upper troposphere (UT), with strong impact on ozone chemistry and the hydroxyl radical production. However, the production efficiency (PE) of lightning nitrogen oxides (LNO<sub>x</sub>) is still quite uncertain (32 – 1100 mol NO per flash). Satellite measurements are a powerful tool to estimate LNO<sub>x</sub> directly as compared to conventional platforms. To apply satellite data in both clean and polluted regions, a new algorithm for calculating LNO<sub>x</sub> has been developed that uses the Berkeley High Resolution (BEHR) v3.0B NO<sub>2</sub> retrieval algorithm and the Weather Research and Forecasting-Chemistry (WRF-Chem) model. LNO<sub>x</sub> PE over the continental US is estimated using the NO<sub>2</sub> product of the Ozone Monitoring Instrument (OMI) data and the Earth Networks Total Lightning Network (ENTLN) data. Focusing on the summer season during 2014, we find that the lightning NO<sub>2</sub> (LNO<sub>2</sub>) PE is  $32 \pm 15$  mol NO<sub>2</sub> flash<sup>-1</sup> and  $6 \pm 3$  mol NO<sub>2</sub> stroke<sup>-1</sup> while LNO<sub>x</sub> PE is  $90 \pm 50$  mol NO<sub>x</sub> flash<sup>-1</sup> and  $17 \pm 10$  mol NO<sub>x</sub> stroke<sup>-1</sup>. Results reveal that our method reduces the sensitivity to the background NO<sub>2</sub> and includes much of the below-cloud LNO<sub>2</sub>. As the LNO<sub>x</sub> parameterization varies in studies, the sensitivity of our calculations to the setting of the amount of lightning NO (LNO) is evaluated. Careful consideration of the ratio of LNO<sub>2</sub> to NO<sub>2</sub> is also needed, given its large influence on the estimation of LNO<sub>2</sub> PE.

## 1 Introduction

Nitrogen oxides (NO<sub>x</sub>) near the Earth's surface are mainly produced by soil, biomass burning and fossil fuel combustion, while NO<sub>x</sub> in the middle and upper troposphere originates largely from lightning and aircraft emissions. NO<sub>x</sub> plays an important role in the production of ozone (O<sub>3</sub>) and the hydroxyl radical (OH). While the anthropogenic sources of NO<sub>x</sub> are largely known, lightning nitrogen oxides (LNO<sub>x</sub>) are still the source with the greatest uncertainty, though they are estimated to range between 2 and 8 Tg N yr<sup>-1</sup> (Schumann and Huntrieser, 2007). LNO<sub>x</sub> is produced in the upper troposphere (UT) by O<sub>2</sub> and N<sub>2</sub> dissociation in the hot lightning channel as described by the Zel'dovich mechanism (Zel'dovich and Raizer, 1967). With the recent updates

of UT  $\text{NO}_x$  chemistry, the day time lifetime of UT  $\text{NO}_x$  is evaluated to be  $\sim 3$  h near thunderstorms and  $\sim 0.5 - 1.5$  days away from thunderstorms (Nault et al., 2016, 2017). This results in enhanced  $\text{O}_3$  production in the cloud outflow of active convection (Pickering et al., 1996; Hauglustaine et al., 2001; DeCaria et al., 2005; Ott et al., 2007; Dobber et al., 2008; Allen et al., 2010; Finney et al., 2016). As  $\text{O}_3$  is known as a greenhouse gas, strong oxidant and absorber of ultraviolet radiation (Myhre et al., 2013), the contributions of  $\text{LNO}_x$  to  $\text{O}_3$  production also have an effect on climate forcing. Finney et al. (2018) found different impacts on atmospheric composition and radiative forcing when simulating future lightning using a new upward cloud ice flux (IFLUX) method versus the commonly used cloud-top height (CTH) approach. While global lightning is predicted to increase by 5 — 16% over the next century with the CTH approach (Clark et al., 2017; Banerjee et al., 2014; Krause et al., 2014), a 15% decrease in global lightning was estimated with IFLUX in 2100 under a strong global warming scenario (Finney et al., 2018). As a result of the different effects on radiative forcing from ozone and methane, a net positive radiative forcing was found with the CTH approach while there is little net radiative forcing with the IFLUX approach (Finney et al., 2018). However, the convective available potential energy (CAPE) times the precipitation rate (P) proxy predicts a  $12 \pm 5\%$  increase in the Continental US (CONUS) lightning strike rate per kelvin of global warming (Romps et al., 2014), while the IFLUX proxy predicts the lightning will only increase 3.4%/K over the CONUS. Recently, Romps (2019) compared the  $\text{CAPE} \times \text{P}$  proxy and IFLUX method in cloud-resolving models. They reported that higher CAPE and updraft velocities caused by global warming could lead to the large increases in tropical lightning simulated by  $\text{CAPE} \times \text{P}$  proxy, while IFLUX proxy predicts little change in tropical lightning because of the small changes in the mass flux of ice.

In the view of the regionally dependent lifetime of  $\text{NO}_x$  and the difficulty of measuring  $\text{LNO}_x$  directly, a better understanding of the  $\text{LNO}_x$  production is required, especially in the tropical and mid-latitude regions in summer. Using its distinct spectral absorption lines in the near-ultraviolet (UV) and visible (VIS) range (Platt and Perner, 1983),  $\text{NO}_2$  can be measured by satellite instruments like the Global Ozone Monitoring Experiment (GOME; Burrows et al., 1999; Richter et al., 2005), Scanning Imaging Absorption Spectrometer for Atmospheric Chartography (SCIAMACHY; Bovensmann et al., 1999), the Second Global Ozone Monitoring Experiment (GOME-2; Callies et al., 2000) and the Ozone Monitoring Instrument (OMI; Levelt et al., 2006). OMI has the highest spatial resolution, least instrument degradation and longest record among these satellites (Krotkov et al., 2017). Satellite measurements of  $\text{NO}_2$  are a powerful tool compared to conventional platforms, because of its global coverage, constant instrument features and temporal continuity.

Recent studies have determined and quantified  $\text{LNO}_x$  using satellite observations. Beirle et al. (2004) constrained the  $\text{LNO}_x$  production to 2.8 (0.8 – 14)  $\text{Tg N yr}^{-1}$  by combining GOME  $\text{NO}_2$  data and flash counts from the Lightning Imaging Sensor (LIS) aboard the Tropical Rainfall Measurement Mission (TRMM) over Australia. Boersma et al. (2005) estimated the global  $\text{LNO}_x$  production of 1.1 – 6.4  $\text{Tg N yr}^{-1}$  by comparing GOME  $\text{NO}_2$  with distributions of  $\text{LNO}_2$  modeled by Tracer Model 3 (TM3). Martin et al. (2007) analyzed SCIAMACHY  $\text{NO}_2$  columns with Goddard Earth Observing System chemistry model (GEOS-Chem) simulations to identify  $\text{LNO}_x$  production amounting to  $6 \pm 2 \text{ Tg N yr}^{-1}$ .

As these methods focus on monthly or annual mean  $\text{NO}_2$  column densities, more recent studies applied specific approaches to investigate  $\text{LNO}_x$  directly over active convection. Beirle et al. (2006) estimated  $\text{LNO}_x$  as 1.7 (0.6 – 4.7)  $\text{Tg N yr}^{-1}$  based on a convective system over the Gulf of Mexico, using National Lightning Detection Network (NLDN) observations and GOME

NO<sub>2</sub> column densities. However, it is assumed that all the enhanced NO<sub>2</sub> originated from lightning and did not consider the contribution of anthropogenic emissions. Beirle et al. (2010) analyzed LNO<sub>x</sub> production systematically using the global dataset of SCIAMACHY NO<sub>2</sub> observations combined with flash data from the World Wide Lightning Location Network (WWLLN). Their analysis was restricted to 30×60 km<sup>2</sup> satellite pixels where the flash rate exceeded 1 flash km<sup>-2</sup> hr<sup>-1</sup>. But they found  
60 LNO<sub>x</sub> production to be highly variable and correlations between flash rate densities and LNO<sub>x</sub> production were low in some cases. Bucselo et al. (2010) estimated LNO<sub>x</sub> production as ~ 100 – 250 mol NO<sub>x</sub>/flash for four cases, using the DC-8 and OMI data during NASA's Tropical Composition, Cloud and Climate Coupling Experiment (TC<sup>4</sup>).

Based on the approach used by Bucselo et al. (2010), a special algorithm was developed by Pickering et al. (2016) to retrieve LNO<sub>x</sub> from OMI and the WWLLN. The algorithm takes the OMI tropospheric slant column density (SCD) of NO<sub>2</sub> (S<sub>NO<sub>2</sub></sub>) as  
65 the tropospheric slant column density of LNO<sub>2</sub> (S<sub>LNO<sub>2</sub></sub>) by using cloud radiance fraction (CRF) greater than 0.9 to minimize or screen the lower tropospheric background. To convert the S<sub>LNO<sub>2</sub></sub> to the tropospheric vertical column density (VCD) of LNO<sub>x</sub> (V<sub>LNO<sub>x</sub></sub>), an air mass factor (AMF) is calculated by dividing the a priori S<sub>LNO<sub>2</sub></sub> by the a priori V<sub>LNO<sub>x</sub></sub>. The a priori S<sub>LNO<sub>2</sub></sub> is calculated using a radiative transfer model and a profile of LNO<sub>2</sub> simulated by the NASA Global Modeling Initiative (GMI) chemical transport model. The a priori V<sub>LNO<sub>x</sub></sub> is also obtained from the GMI model. Results for the Gulf of Mexico during  
70 2007 – 2011 summer yield LNO<sub>x</sub> production of 80 ± 45 mol NO<sub>x</sub> per flash. Since they considered NO<sub>2</sub> above the cloud as LNO<sub>2</sub> in the algorithm due to the difficulty and uncertainty in determining the background NO<sub>2</sub>, their AMF and derived VCD of LNO<sub>x</sub> (LNO<sub>2</sub>) is named as AMF<sub>LNO<sub>x</sub>Clean</sub> (AMF<sub>LNO<sub>2</sub>Clean</sub>) and LNO<sub>x</sub>Clean (LNO<sub>2</sub>Clean), respectively. Note that Pickering et al. (2016) considered the two estimates of background derived from aircraft flights in the Gulf of Mexico region (3% and 33%) and subtracted the mean value (18%) from the estimated mean LNO<sub>x</sub> production efficiency (PE) for the background  
75 bias. However, we use the original algorithm directly without correction to distinguish the effect of different AMFs on LNO<sub>x</sub> estimation in the remainder of this paper. Unless otherwise specified, abbreviations S and V are respectively defined as the tropospheric SCD and VCD in this paper.

More recently Bucselo et al. (2019) obtained an average PE of 180 ± 100 mol NO<sub>x</sub>/flash over East Asia, Europe and North America based on a modification of the method used in Pickering et al. (2016). A power function between LNO<sub>x</sub> and lightning  
80 flash rate was established, while the minimum flash-rate threshold was not applied. The tropospheric NO<sub>x</sub> background was removed by subtracting the temporal average of NO<sub>x</sub> at each box where the value was weighted by the number of OMI pixels which meet the optical cloud pressure and CRF criteria required to be considered deep convection but have 1 flash or less instead. The lofted pollution was considered as 15% of total NO<sub>x</sub> according to the estimation from DeCaria et al. (2000, 2005) and the average chemical delay was adjusted by 15% following the 3-hour LNO<sub>x</sub> lifetime in the nearby field of convection  
85 (Nault et al., 2017). However, there were negative LNO<sub>x</sub> values caused by the overestimation of the tropospheric background and stratospheric NO<sub>2</sub> at some locations.

On the other hand, Lapierre et al. (2020) constrained LNO<sub>2</sub> to 1.1 ± 0.2 mol NO<sub>2</sub>/stroke for intracloud (IC) strokes and 10.7 ± 2.5 mol NO<sub>2</sub>/stroke for cloud-to-ground (CG) strokes over the CONUS. LNO<sub>2</sub> per stroke was scaled to 24.2 mol NO<sub>x</sub>/flash using mean values of strokes per flash and the ratio of NO<sub>x</sub> to NO<sub>2</sub> in the UT. They used the regrided Berkeley  
90 High-Resolution (BEHR) V3.0A 0.05° × 0.05° "visible only" NO<sub>2</sub> VCD (V<sub>vis</sub>) product which includes two parts of NO<sub>2</sub> that

can be "seen" by the satellite. The first part is the NO<sub>2</sub> above clouds (pixels with CRF > 0.9) and the second part is the NO<sub>2</sub> detected from cloud free areas. A threshold of  $3 \times 10^{15}$  molecules cm<sup>-2</sup>, the typical urban NO<sub>2</sub> concentration, was applied to mask the contaminated grid cells (Beirle et al., 2010; Laughner and Cohen, 2017). The main difference between Lapierre et al. (2020) and Pickering et al. (2016) is the air mass factor for lightning (AMF<sub>LNO<sub>x</sub></sub>) implemented in the basic algorithm.

95 In Lapierre et al. (2020), the air mass factor was used to convert S<sub>NO<sub>2</sub></sub> to V<sub>vis</sub>, while in Pickering et al. (2016) it was used to convert S<sub>LNO<sub>2</sub></sub> to V<sub>LNO<sub>x</sub></sub>, assuming that all S<sub>NO<sub>2</sub></sub> is generated by lightning.

To apply the approach used by Bucsele et al. (2010), Pickering et al. (2016), Bucsele et al. (2019) and Lapierre et al. (2020) without geographic restrictions, the contamination by anthropogenic emissions must be taken into account in detail. The Weather Research and Forecasting (WRF) model coupled with chemistry (WRF-Chem) has been employed to evaluate

100 the convective transport and chemistry in many studies (Barth et al., 2012; Wong et al., 2013; Fried et al., 2016; Li et al., 2017). Meanwhile, Laughner and Cohen (2017) showed that the OMI AMF is increased by ~35% for summertime when LNO<sub>2</sub> simulated by WRF-Chem is included in the a priori profiles to match aircraft observations. The simulation agrees with observed NO<sub>2</sub> profiles and the bias of AMF related to these observations is reduced to < ±4% for OMI viewing geometries.

In this paper, we focus on the estimation of LNO<sub>2</sub> production per flash (LNO<sub>2</sub>/flash), LNO<sub>x</sub> production per flash (LNO<sub>x</sub>/flash),

105 LNO<sub>2</sub> production per stroke (LNO<sub>2</sub>/stroke) and LNO<sub>x</sub> production per stroke (LNO<sub>x</sub>/stroke) in May–August (MJJA) 2014 by developing an algorithm similar to Pickering et al. (2016) based on the BEHR NO<sub>2</sub> retrieval algorithm (Laughner et al., 2018a, b), but it performs better over background NO<sub>2</sub> sources. Section 2 describes the satellite data, lightning data, model settings and the algorithm in detail. Section 3 explores the suitable data criteria, compares different methods and evaluates the effect of background NO<sub>2</sub>, cloud and LNO<sub>x</sub> parameterization on LNO<sub>x</sub> production estimation. Section 4 examines the effect of different

110 sources of the uncertainty on the results. Conclusions are summarized in Section 5.

## 2 Data and Methods

### 2.1 Ozone Monitoring Instrument (OMI)

OMI is carried on the Aura satellite (launched in 2004), a member of A-train satellite group (Levelt et al., 2006, 2018). OMI passes over the equator at ~ 13:45 LT (ascending node) and has a swath width of 2600 km, with a nadir field-of-view resolution

115 of  $13 \times 24$  km<sup>2</sup>. Since the beginning of 2007, some of the measurements have become useless as a result of anomalous radiances called the "row anomaly" (Dobber et al., 2008; KNMI, 2012). For the current study, we used the NASA standard product V3.0 (Krotkov et al., 2017) as input to the LNO<sub>x</sub> retrieval algorithm.

The main steps of calculating the NO<sub>2</sub> tropospheric VCD (V<sub>NO<sub>2</sub></sub>) in the NASA product include:

1. SCDs are determined by the OMI-optimized differential optical absorption spectroscopy (DOAS) spectral fit;
- 120 2. A corrected ("de-striped") SCD is obtained by subtracting the cross-track bias caused by an instrument artifact from the measured slant column;

3. The AMF for stratospheric ( $AMF_{strat}$ ) or tropospheric column ( $AMF_{trop}$ ) is calculated from the  $NO_2$  profiles integrated vertically using weighted scattering weights with the a priori profiles. These profiles are obtained from GMI monthly mean profiles using four years (2004 – 2007) simulation;

125 4. The stratospheric  $NO_2$  VCD ( $V_{strat}$ ) is calculated from the subtraction of a priori contribution from tropospheric  $NO_2$  and a three-step (interpolation, filtering, and smoothing) algorithm (Bucsela et al., 2013);

5.  $V_{strat}$  is converted to the slant column using  $AMF_{strat}$  and subtracted from the measured SCDs to yield  $S_{NO_2}$ , leading to  $V_{NO_2} = S_{NO_2}/AMF_{trop}$ .

130 Based on this method, we developed a new  $AMF_{LNO_x}$  to obtain the desired  $V_{LNO_x}$  ( $V_{LNO_x} = S_{NO_2}/AMF_{LNO_x}$ ) by replacing the original step 5. Details of this algorithm are discussed in section 2.4.

## 2.2 The Earth Networks Total Lightning Detection Network (ENTLN)

The Earth Networks Total Lightning Network (ENTLN) operates a system of over 1500 ground-based stations around the world with more than 900 sensors installed in the CONUS (Zhu et al., 2017). Both IC and CG lightning flashes are located by the sensors with detection frequency ranging from 1 Hz to 12 MHz based on the electric field pulse polarity and wave shapes.  
135 Groups of pulses are classified as a flash if they are within 700 ms and 10 km. In the preprocessed data obtained from the ENTLN, both strokes and lightning flashes composed of one or more strokes are included.

Rudlosky (2015) compared ENTLN combined events (IC and CG) with LIS flashes and found that the relative flash detection efficiency of ENTLN over CONUS increases from 62.4% during 2011 to 79.7% during 2013. Lapierre et al. (2020) also compared combined ENTLN and the NLDN dataset with data from the LIS during 2014 and found the detection efficiencies  
140 of IC flashes and strokes to be 88% and 45%, respectively. Since we only use the ENTLN data in 2014 as Lapierre et al. (2020) and NLDN detection efficiency of IC pulses should be lower than 33% which is calculated by the data in 2016 (Zhu et al., 2016), only the IC flashes and strokes are divided by 0.88 and 0.45, respectively, while CG flashes and strokes are unchanged because of the high detection efficiency.

## 2.3 Model Description

145 The present study uses WRF-Chem version 3.5.1 (Grell et al., 2005) with a horizontal grid size of  $12 \times 12$  km<sup>2</sup> and 29 vertical levels (Fig. 1). The initial and boundary conditions of meteorological parameters are provided by the North American Regional Reanalysis (NARR) dataset with a 3 hourly time resolution. Based on Laughner et al. (2018b), 3D wind fields, temperature and water vapor are nudged towards the NARR data. Outputs from the version 4 of Model for Ozone and Related chemical Tracers (MOZART-4; Emmons et al., 2010) are used to generate the initial and boundary conditions of chemical species. Anthropogenic  
150 emissions are driven by the 2011 National Emissions Inventory (NEI), scaled to model years by the Environmental Protection Agency annual total emissions (EPA and OAR, 2015). The Model of Emissions of Gases and Aerosol from Nature (MEGAN; Guenther et al., 2006) is used for biogenic emissions. The chemical mechanism is the version 2 of Regional Atmospheric Chemistry Mechanism (RACM2; Goliff et al., 2013) with updates from Browne et al. (2014) and Schwantes et al. (2015). In addition, lightning flash rate based on the level of neutral buoyancy parameterization (Price and Rind, 1992; Wong et al., 2013)

155 and  $LNO_x$  parameterizations are activated (200 mol NO flash<sup>-1</sup>, the factor to adjust the predicted number of flashes is set to 1; hereinafter referred to as "1×200 mol NO flash<sup>-1</sup>"). Simulated total flash densities are higher than ENTLN observations over the Southeast US and lower than observations in the North Central US (Fig. 2). The impact of these biases on  $LNO_x$  production is discussed and mitigated in Sect. 3.1 and 3.4. The bimodal profile modified from the standard Ott et al. (2010) profile (Laughner and Cohen, 2017) is employed as the vertical distribution of lightning NO (LNO) in WRF-Chem, while  
 160 outputs of LNO and  $LNO_2$  profiles are defined as the difference of vertical profiles between simulations with and without lightning.

## 2.4 Method for Deriving AMF

The  $V_{LNO_x}$  near convection is calculated according:

$$V_{LNO_x} = \frac{S_{NO_2}}{AMF_{LNO_x}} \quad (1)$$

165 where  $S_{NO_2}$  is the OMI-measured tropospheric slant column  $NO_2$  and  $AMF_{LNO_x}$  is a customized lightning air mass factor. The concept of  $AMF_{LNO_x}$  was also used in Beirle et al. (2009) to investigate the sensitivity of satellite instruments to freshly produced lightning  $NO_x$ . In order to estimate  $LNO_x$ , we define the  $AMF_{LNO_x}$  as the ratio of the "visible" modeled  $NO_2$  slant column to the total modeled tropospheric  $LNO_x$  vertical column (derived from the a priori NO and  $NO_2$  profiles, scattering weights, and cloud radiance fraction):

$$170 \quad AMF_{LNO_x} = \frac{(1 - f_r) \int_{p_{surf}}^{p_{tp}} w_{clear}(p) NO_2(p) dp + f_r \int_{p_{cloud}}^{p_{tp}} w_{cloudy}(p) NO_2(p) dp}{\int_{p_{surf}}^{p_{tp}} LNO_x(p) dp} \quad (2)$$

where  $f_r$  is the cloud radiance fraction (CRF),  $p_{surf}$  is the surface pressure,  $p_{tp}$  is the tropopause pressure,  $p_{cloud}$  is the cloud optical pressure (CP),  $w_{clear}$  and  $w_{cloudy}$  are respectively the pressure dependent scattering weights from the TOMRAD lookup table (Bucsela et al., 2013) for clear and cloudy parts, and  $NO_2(p)$  is the modeled  $NO_2$  vertical profile. Details of these standard parameters and calculation methods are given in Laughner et al. (2018a).  $LNO_x(p)$  is the  $LNO_x$  vertical profile calculated by  
 175 the difference of vertical profiles between WRF-Chem simulations with and without lightning.

Please note that the CP is a reflectance-weighted pressure retrieved by the collision-induced  $O_2-O_2$  absorption band near 477 nm (Acarreta et al., 2004; Sneep et al., 2008; Stammes et al., 2008). For a deep convective cloud with lightning, the CP lies below the geometrical cloud top which is much closer to that detected by thermal infrared sensors, such as the CloudSat and the Aqua MODerate-resolution Imaging Spectrometer (MODIS) (Vasilkov et al., 2008; Joiner et al., 2012). Hence, much of  
 180 the tropospheric  $NO_2$  measured by OMI lies inside the cloud rather than above the cloud top. In the following, "above cloud" or "below cloud" is relative to the cloud pressure detected by OMI. The sensitivity study of Beirle et al. (2009) compared the chemical composition from the cloud bottom to the cloud top and revealed that a significant fraction of the  $NO_2$  within the cloud originating from lightning can be detected by the satellite. This valuable cloud pressure concept has been applied not only in the  $LNO_x$  research but also in the cloud slicing method of deriving the UT  $O_3$  and  $NO_x$  (Ziemke et al., 2009; Choi et al.,  
 185 2014; Strode et al., 2017; Ziemke et al., 2017; Marais et al., 2018). As discussed in Pickering et al. (2016), the ratio of  $V_{LNO_2}$  seen by OMI to  $V_{LNO_x}$  is partly influenced by  $p_{cloud}$ . The effects of  $LNO_2$  below the cloud will be discussed in Sect. 3.4.

To compare our results with those of Pickering et al. (2016) and Lapierre et al. (2020), we calculate their  $AMF_{LNO_x \text{Clean}}$  and  $AMF_{NO_2 \text{Vis}}$  respectively:

$$AMF_{LNO_x \text{Clean}} = \frac{(1 - f_r) \int_{p_{\text{surf}}}^{p_{\text{tp}}} w_{\text{clear}}(p) LNO_x(p) dp + f_r \int_{p_{\text{cloud}}}^{p_{\text{tp}}} w_{\text{cloudy}}(p) LNO_x(p) dp}{\int_{p_{\text{surf}}}^{p_{\text{tp}}} LNO_x(p) dp} \quad (3)$$

190

$$AMF_{NO_2 \text{Vis}} = \frac{(1 - f_r) \int_{p_{\text{surf}}}^{p_{\text{tp}}} w_{\text{clear}}(p) NO_2(p) dp + f_r \int_{p_{\text{cloud}}}^{p_{\text{tp}}} w_{\text{cloudy}}(p) NO_2(p) dp}{(1 - f_g) \int_{p_{\text{surf}}}^{p_{\text{tp}}} NO_2(p) dp + f_g \int_{p_{\text{cloud}}}^{p_{\text{tp}}} NO_2(p) dp} \quad (4)$$

where  $f_g$  is the geometric cloud fraction and  $LNO_x(p)$  is the modeled  $LNO_x$  vertical profile. Besides these AMFs, another AMF called  $AMF_{LNO_2 \text{Vis}}$  is developed for later comparison.

$$AMF_{LNO_2 \text{Vis}} = \frac{(1 - f_r) \int_{p_{\text{surf}}}^{p_{\text{tp}}} w_{\text{clear}}(p) NO_2(p) dp + f_r \int_{p_{\text{cloud}}}^{p_{\text{tp}}} w_{\text{cloudy}}(p) NO_2(p) dp}{(1 - f_g) \int_{p_{\text{surf}}}^{p_{\text{tp}}} LNO_2(p) dp + f_g \int_{p_{\text{cloud}}}^{p_{\text{tp}}} LNO_2(p) dp} \quad (5)$$

195 A full definition list of the used AMFs is shown in Appendix A.

## 2.5 Procedures for Deriving $LNO_x$

$V_{LNO_x}$  is re-gridded to  $0.05^\circ \times 0.05^\circ$  grids using the constant value method (Kuhlmann et al., 2014). Then, it is analyzed in  $1^\circ \times 1^\circ$  grid boxes with a minimum of fifty valid  $0.05^\circ \times 0.05^\circ$  grids to minimize the noise. The main procedures of deriving  $LNO_x$  are as follows:

200 CRFs ( $CRF \geq 70\%$ ,  $CRF \geq 90\%$  and  $CRF = 100\%$ ) and  $CP \leq 650$  hPa are various criteria of deep convective clouds for OMI pixels (Ziemke et al., 2009; Choi et al., 2014; Pickering et al., 2016). The effect of different CRFs on the retrieved  $LNO_x$  is explored in section 3.2. Furthermore, another criterion of cloud fraction (CF) is applied to the WRF-Chem results for the successful simulation of convection. The CF is defined as the maximum cloud fraction calculated by the Xu-Randall method between 350 and 400 hPa (Xu and Randall, 1996; Strode et al., 2017). This atmospheric layer (between 350 and 400 hPa)  
205 avoids any biases in the simulation of high clouds. We choose  $CF \geq 40\%$  suggested by Strode et al. (2017) to determine cloudy or clear for each simulation grid.

Besides cloud properties, a time period and sufficient flashes (or strokes) are required for fresh  $LNO_x$  to be detected by OMI. The time window ( $t_{\text{window}}$ ) is the hours prior to the OMI overpass time.  $t_{\text{window}}$  is limited to 2.4 h by the mean wind speed at pressure levels 500 – 100 hPa during OMI overpass time and the square root of the  $1^\circ \times 1^\circ$  box over the CONUS (Lapierre  
210 et al., 2020). Meanwhile, 2400 flashes  $\text{box}^{-1}$  and 8160 strokes  $\text{box}^{-1}$  per 2.4 hour time window are chosen as sufficient for detecting  $LNO_x$  (Lapierre et al., 2020). These criteria will result in a low bias in the PE results, as Bucselo et al. (2019) found that the PE is larger at small flash rates which are discarded here. Since our study focuses on developing a new AMF and compare results with other works using the similar lightning thresholds (Lapierre et al., 2020; Pickering et al., 2016), we will only discuss results based on the strict criteria in the main text. For comparisons between 2400 flashes  $\text{box}^{-1}$  criterion and 1  
215 flash  $\text{box}^{-1}$  criterion, scatter diagrams using different lightning criteria are presented in Appendix B.

To ensure that lightning flashes are simulated successfully by WRF-Chem, the threshold of simulated total lightning flashes (TL) per box is set to 1000, which is fewer than that used by the ENTLN lightning observation, considering the uncertainty of lightning parameterization. In view of other NO<sub>2</sub> sources in addition to LNO<sub>2</sub>, the ratio of modeled lightning NO<sub>2</sub> above cloud (LNO<sub>2</sub>Vis) to modeled NO<sub>2</sub> above cloud (NO<sub>2</sub>Vis) is defined to check whether enough LNO<sub>2</sub> can be detected by OMI. The ratio  $\geq 50\%$  indicates that more than half of the NO<sub>x</sub> above the cloud must have an LNO<sub>x</sub> source.

Finally, the NO<sub>2</sub> lifetime against oxidation should be taken into account. As estimated by Nault et al. (2016), the lifetime ( $\tau$ ) of NO<sub>2</sub> in the near field of convections is  $\sim 3$  h. The initial value of NO<sub>2</sub> is solved by Eq. 6 as

$$NO_2(0) = NO_2(OMI) \times e^{0.5t/\tau} \quad (6)$$

where  $NO_2(0)$  is the moles of NO<sub>2</sub> emitted at time  $t = 0$ ,  $NO_2(OMI)$  is the moles of NO<sub>2</sub> measured at the OMI overpass time and  $0.5t$  is the half cross grid time which is 1.2 h, assuming that lightning occurred at the center of each  $1^\circ \times 1^\circ$  box. For each grid box, the mean LNO<sub>x</sub> vertical column is obtained by averaging  $V_{LNO_x}$  values from all regridded  $0.05^\circ \times 0.05^\circ$  pixels in the box. This mean value is converted to moles LNO<sub>x</sub> using the dimensions of the grid box. Two methods are applied to estimate the seasonal mean LNO<sub>2</sub>/flash, LNO<sub>x</sub>/flash, LNO<sub>2</sub>/stroke and LNO<sub>x</sub>/stroke:

- (1) summation method: dividing the sum of LNO<sub>x</sub> by the sum of flashes (or strokes) in each  $1^\circ \times 1^\circ$  box in MJJA 2014;
- (2) linear regression method: applying the linear regression to daily mean values of LNO<sub>x</sub> and flashes (or strokes).

### 3 Results

#### 3.1 Criteria Determination

To determine the suitable criteria from conditions defined in section 2.5, six different combinations are defined (Table 1) and applied to the original data with a linear regression method (Table 2).

A daily search of the NO<sub>2</sub> product for coincident ENTLN flash (stroke) data results in 99 (102) valid days under the CRF90\_ENTLN condition. Taking the flash type ENTLN data as an example, the number of valid days decreases from 99 to 81 under the CRF90\_ENTLN\_TL1000\_ratio50 condition, while LNO<sub>x</sub>/flash increases from  $52.1 \pm 51.1$  mol/flash to  $54.5 \pm 48.1$  mol/flash. The result is almost the same as that under the CRF90\_ENTLN\_TL1000 condition which is without the condition of more than half of the above-cloud NO<sub>x</sub> having an LNO<sub>x</sub> source. Although this indicates the criterion of TL works well, it is better to include the ratio criterion in case of some exceptions in the different AMF methods. Since  $CF \geq 40\%$  leads to a sharp loss of valid numbers and production, therefore, it is not a suitable criterion. Instead the CRF criteria are used. Finally, coincident ENTLN data,  $TL \geq 1000$  and  $ratio \geq 50\%$  are chosen as the thresholds to explore the effects of three different CRF conditions ( $CRF \geq 70\%$ ,  $CRF \geq 90\%$  and  $CRF = 100\%$ ) on LNO<sub>x</sub> production (Table 3). Apart from the fewer valid days under higher CRF conditions ( $CRF \geq 90\%$  and  $CRF = 100\%$ ), LNO<sub>x</sub>/flash increases from  $35.7 \pm 36.8$  mol/flash to  $54.5 \pm 48.1$  mol/flash and decreases again to  $20.8 \pm 37.4$  mol/flash while LNO<sub>x</sub>/stroke enhances from  $4.1 \pm 3.9$  mol/stroke to  $7.0 \pm 4.8$  mol/stroke and drops again to  $2.6 \pm 4.0$  mol/stroke (Table 3), as the CRF criterion increases from 70% to 90% and to 100%. When the CRF increases from 90% to 100%, the LNO<sub>x</sub> PE decreases because of the higher lightning density with



fewer LNO<sub>x</sub> (not shown). The increment of LNO<sub>x</sub> PE caused by the CRF increase from 70% to 90% is opposite to the result of Pickering et al. (2016). This is an effect of the consideration of NO<sub>2</sub> contamination transported from the boundary layer in our method. Although enhanced NO<sub>x</sub> is often observed in regions with CRF > 70% (Pickering et al., 2016), the following analysis will be based on the criterion of CRF ≥ 90% considering the contamination by low and mid-level NO<sub>2</sub> and comparisons with the results of Pickering et al. (2016) and Lapierre et al. (2020).

### 3.2 Comparison of LNO<sub>x</sub> Production based on Different AMFs

Lapierre et al. (2020) derived LNO<sub>2</sub> production based on the BEHR NO<sub>2</sub> product. In order for our results to be comparable with those of Pickering et al. (2016) and Lapierre et al. (2020), we choose NO<sub>2</sub> instead of NO<sub>x</sub> to derive production per flash (production efficiency, PE). In Fig. 3, time series of NO<sub>2</sub>Vis, LNO<sub>2</sub>Vis, LNO<sub>2</sub> and LNO<sub>2</sub>Clean production per day over CONUS are plotted for MJJA 2014 with the criterion of CRF ≥ 90% and a flash threshold of 2400 flashes per 2.4 h. LNO<sub>2</sub> PEs are mostly in the range from 20 to 80 mol/flash. LNO<sub>2</sub>Vis PEs are smaller than LNO<sub>2</sub> PEs which contain LNO<sub>2</sub> below clouds. The simulation of GMI in Pickering et al. (2016) indicated that 25% – 30% of the LNO<sub>x</sub> column lies below the CP, while the ratio in our WRF-Chem simulation is 56 ± 20%. The effect of cloud properties on LNO<sub>x</sub> PE will be discussed in more detail in section 3.4. Generally, the order of estimated daily PEs is LNO<sub>2</sub>Clean > LNO<sub>2</sub> > NO<sub>2</sub>Vis > LNO<sub>2</sub>Vis. The percent difference in the estimated PE (ΔPE) between NO<sub>2</sub>Vis and LNO<sub>2</sub>Vis indicates a certain amount of background NO<sub>2</sub> exists above clouds. Overall, the tendency of that ΔPE is consistent with another ΔPE between NO<sub>2</sub>Vis and LNO<sub>2</sub>Clean. When the region is highly polluted (ΔPE between NO<sub>2</sub>Vis and LNO<sub>2</sub>Vis is larger than 200%), PEs based on NO<sub>2</sub>Vis and LNO<sub>2</sub>Clean are significantly overestimated. In other words, NO<sub>2</sub>Vis and LNO<sub>2</sub>Clean are more sensitive to background NO<sub>2</sub>. The extent of the overestimation of NO<sub>2</sub>Vis is larger than that of LNO<sub>2</sub>Clean in highly polluted regions, while it is usually opposite in most regions.

Figure 4 shows the linear regression for ENTLN data versus NO<sub>2</sub>Vis, LNO<sub>2</sub>Vis, LNO<sub>2</sub> and LNO<sub>2</sub>Clean with the same criteria as shown in Fig. 3. LNO<sub>2</sub>Clean PE (the largest slope) is 25.2 ± 22.3 mol NO<sub>2</sub>/flash with a correlation of 0.25 and 2.3 ± 2.1 mol NO<sub>2</sub>/stroke with a correlation of 0.22. As shown in Fig. 3, positive percent differences between NO<sub>2</sub>Vis PE and LNO<sub>2</sub>Clean PE occur much fewer than negative differences. As a result, NO<sub>2</sub>Vis PE (17.1 ± 17.2 mol NO<sub>2</sub>/flash and 0.4 ± 1.0 mol NO<sub>2</sub>/stroke) is smaller than LNO<sub>2</sub>Clean PE using the linear regression method.

In order to compare our result with that of Lapierre et al. (2020), we tried to remove the CP ≤ 650 hPa, TL ≥ 1000 and ratio ≥ 50% conditions from criteria. But, our result based on daily summed NO<sub>2</sub>Vis values (3.8 ± 0.5 mol/stroke) is still larger than the value of 1.6 ± 0.1 mol/stroke mentioned in Lapierre et al. (2020). This may be caused by the different version of BEHR algorithm, as Lapierre et al. (2020) used BEHR V3.0A and our algorithm is based on BEHR V3.0B (Laughner et al., 2019). The input of S<sub>NO<sub>2</sub></sub> in both versions is from the NASA standard product V3 and the major improvements of BEHR V3.0B are listed below:

1. The profile (V3.0B) closest to the OMI overpass time was selected instead of the last profile (V3.0A) before the OMI overpass.

2. The AMF uses a variable tropopause height as opposed to the fixed 200 hPa tropopause.

3. The surface pressure is now calculated according to Zhou et al. (2009).

The detailed log of changes is available at <https://github.com/CohenBerkeleyLab/BEHR-core> (last access: March 8, 2020). Note that Lapierre et al. (2020) used the monthly NO<sub>2</sub> profile, while the daily profile is used in our study and the interval of our  
285 outputs from WRF-Chem is 30 min which is more frequent than 1 h in the BEHR daily product, the AMF could be affected by different NO<sub>2</sub> profiles. In view of these factors, we compare different methods based on our data to minimize these effects.

Meanwhile, LNO<sub>2</sub> PE (18.7 ± 18.1 mol/flash and 2.1 ± 1.8 mol/stroke) is between LNO<sub>2</sub>Clean PE and NO<sub>2</sub>Vis PE, which coincides with the daily results in Fig. 3. Furthermore, the LNO<sub>x</sub> PE based on the linear regression of daily summed values, the same method used in Pickering et al. (2016), is 114.8 ± 18.2 mol/flash (or 17.8 ± 2.9 mol/stroke) which is larger than 91  
290 mol/flash in Pickering et al. (2016), possibly due to the differences in geographic location, lightning data and chemistry model.

The mean and standard deviation of LNO<sub>2</sub> PE under CRF ≥ 90% using the summation method is 46.2 ± 35.1 mol/flash and 9.9 ± 8.1 mol/stroke, while LNO<sub>x</sub> PE is 125.6 ± 95.9 mol/flash and 26.7 ± 21.6 mol/stroke (Fig. 5). The LNO<sub>2</sub> PE and LNO<sub>x</sub> PE are both higher in the Southeast U.S. (denoted by the red box in Fig. 5 panels, 75°W – 95°W, 25°N – 37°N), consistent with Lapierre et al. (2020) and Bucsela et al. (2019). Compared with Fig. 3, Figure 6a and b present some large  
295 differences between NO<sub>2</sub>Vis PE and LNO<sub>2</sub>Vis PE, which are consistent with what we expect for polluted regions. Meanwhile, the differences between LNO<sub>2</sub> PE and NO<sub>2</sub>Vis PE depend on background NO<sub>2</sub>, the strength of updraft and the profile. The negative differences are caused by background NO<sub>2</sub> carried by the updraft while parts of the below-cloud LNO<sub>2</sub> result in LNO<sub>2</sub> PE higher than NO<sub>2</sub>Vis PE (Fig. 6c). Figure 6d shows that the ratio of LNO<sub>2</sub>Vis to LNO<sub>2</sub> ranges from 10% – 80%. This may be caused by the height of the clouds and the profile of LNO<sub>2</sub>. If the CP is near 300 hPa, the ratio should be smaller because of  
300 the coverage of clouds. While peaks of the LNO<sub>2</sub> profile are below the CP, the ratio would also be smaller. Therefore, a better understanding of LNO<sub>2</sub> profile and LNO<sub>x</sub> below clouds is required.

### 3.3 Effects of Tropospheric Background on LNO<sub>x</sub> Production

With respect to the LNO<sub>2</sub> production, the patterns in Fig. 6 indicate the improvement of our approach is different in polluted and clean regions. To simplify the quantification, we select six grids with similar NO<sub>2</sub> profile (~ 100 pptv) above the cloud  
305 with CRF = 100%. These grid boxes contain the polluted and clean cities denoted by stars and triangles in Fig. 6a, respectively. Then, the differences between AMFs are dependent on fewer parameters:

$$AMF_{LNO_2} = \frac{\int_{p_{cloud}}^{p_{tp}} w_{cloudy}(p) NO_2(p) dp}{\int_{p_{surf}}^{p_{tp}} LNO_2(p) dp} \quad (7)$$

$$AMF_{NO_2Vis} = \frac{\int_{p_{cloud}}^{p_{tp}} w_{cloudy}(p) NO_2(p) dp}{\int_{p_{cld}}^{p_{tp}} NO_2(p) dp} \quad (8)$$

$$AMF_{LNO_2Clean} = \frac{\int_{p_{cloud}}^{p_{tp}} w_{cloudy}(p) LNO_2(p) dp}{\int_{p_{surf}}^{p_{tp}} LNO_2(p) dp} \quad (9)$$

310 Figure 7 compares the mean profiles of NO<sub>2</sub>, background NO<sub>2</sub> and background NO<sub>2</sub> ratio in polluted and clean grids. Generally, the profiles of the ratio of background NO<sub>2</sub> over total NO<sub>2</sub> are C-shape because UT LNO<sub>2</sub> concentrations are higher than UT background NO<sub>2</sub> concentrations. However, the ratio profile in Fig. 7e has one peak between the cloud pressure and tropopause as background NO<sub>2</sub> increases and LNO<sub>2</sub> decreases. Besides, the percentage of UT background NO<sub>2</sub> in polluted regions is steady and higher than that in clean regions.

315 Table 4 presents the relative changes among three methods in six cities. The difference between AMF<sub>LNO<sub>2</sub></sub> (Eq. 7) and AMF<sub>LNO<sub>2</sub>Clean</sub> (Eq. 9) is the numerator:  $\int_{p_{cloud}}^{p_{vp}} w_{cloudy}(p)NO_2(p) dp$  and  $\int_{p_{cloud}}^{p_{vp}} w_{cloudy}(p)LNO_2(p) dp$ . When the ratio of LNO<sub>2</sub> is higher or the region is cleaner, the relative difference is smaller (e.g. 5.0% – 12.0%, Fig. 7d – f). The largest relative difference (46.3%) occurs when the ratio of background NO<sub>2</sub> is continuously high in the UT (Fig. 7c). As a result, our approach is less sensitive to background NO<sub>2</sub> and more suitable for convective cases over polluted locations. In contrast, production estimated by our method is larger than that based on NO<sub>2</sub>Vis due to the LNO<sub>2</sub> below the cloud. When the cloud is higher, especially the peak of LNO profile is lower than the cloud (Fig. 7b), the relative difference is larger (121.2%) because more LNO<sub>2</sub> can not be included into the NO<sub>2</sub>Vis, which has been discussed in Sect. 3.2. The relative change between AMF<sub>LNO<sub>2</sub>Clean</sub> (Eq. 9) and AMF<sub>NO<sub>2</sub>Vis</sub> (Eq. 8) depends on  $\int_{p_{cloud}}^{p_{vp}} w_{cloudy}(p)LNO_2(p) dp / \int_{p_{surf}}^{p_{vp}} w_{cloudy}(p)LNO_2(p) dp$ , which is also affected by cloud not the background NO<sub>2</sub>. The largest relative change (153.8%) occurs at New Orleans, which has the lowest cloud pressure and consequently the smallest visible column.

### 3.4 Effects of Cloud and LNO<sub>x</sub> Parameterization on LNO<sub>x</sub> Production

Figure 8a presents the daily distribution of CP and the ratio of LNO<sub>2</sub>Vis to LNO<sub>2</sub> during MJJA 2014 with the criteria defined in section 3.1 under CRF  $\geq 90\%$ . Since the ratio of LNO<sub>2</sub>Vis to LNO<sub>2</sub> decreases from 0.8 to 0.2 as the cloud pressure decreases from 600 to 300 hPa, NO<sub>2</sub>Vis PE is smaller than LNO<sub>2</sub> PE in relatively clean areas as shown in Fig. 4. Apart from LNO<sub>2</sub>Vis, the LNO<sub>2</sub> PE is also affected by CP. For LNO<sub>2</sub> PEs larger than 30 mol/stroke, the CPs are all smaller than 550 hPa (Fig. 8b). However, smaller LNO<sub>2</sub> PEs (< 30 mol/stroke) occur on all levels between 650 hPa and 200 hPa. Because of the limited amount of large LNO<sub>2</sub> PEs and lightning data, we cannot derive the relationship between LNO<sub>2</sub> PE and cloud pressure or other lightning properties at this stage. Because the CP only represents the development of clouds, the vertical structure of flashes can not be derived from the CP values only. As discussed in several previous studies, the flash channel length varies and depends on the environmental conditions (Carey et al., 2016; Mecikalski and Carey, 2017; Fuchs and Rutledge, 2018). Davis et al. (2019) compared two kinds of flash: normal flashes and anomalous flashes. Because updrafts are stronger and flash rates are higher in anomalous storms, UT LNO<sub>x</sub> concentrations are larger in anomalous than normal polarity storms. In general, normal flashes are coupled with an upper-level positive charge region and a mid-level negative charge region, while anomalous flashes are opposite (Williams, 1989). It is not straightforward to estimate the error resulting from the vertical distribution of LNO<sub>x</sub>. There are mainly two methods of distributing LNO<sub>x</sub> in models: LNO<sub>x</sub> profiles (postconvection) in which LNO<sub>x</sub> has already been redistributed by convective transport, while the other one (preconvection) uses LNO<sub>x</sub> production profiles made before the redistribution of convective transport (Allen et al., 2012; Luo et al., 2017). However, given the similarity of results

compared to other LNO<sub>x</sub> studies, we believe that our 1° × 1° results based on postconvective LNO<sub>x</sub> profile are sufficient for estimating average LNO<sub>x</sub> production.

345 The LNO production settings in WRF-Chem varied in different studies. Zhao et al. (2009) set a NO<sub>x</sub> production rate of 250 mol NO per flash in a regional-scale model, while Bela et al. (2016) chose 330 mol NO per flash used by Barth et al. (2012). Wang et al. (2015) assumed approximately 500 mol NO per flash which was derived by a cloud-scale chemical transport model and in-cloud aircraft observations (Ott et al., 2010). To illustrate the impact of LNO<sub>x</sub> parameterization on LNO<sub>x</sub> estimation, we apply another WRF-Chem NO<sub>2</sub> profile setting (2×base flashrate, 500 mol NO flash<sup>-1</sup>; hereinafter referred to as "2×500  
350 mol NO flash<sup>-1</sup>") to a priori profiles and evaluate the changes in AMF<sub>LNO<sub>2</sub></sub>, AMF<sub>LNO<sub>x</sub></sub>, LNO<sub>2</sub> PE and LNO<sub>x</sub> PE. For the linear regression method (Fig. 9), LNO<sub>2</sub> PE is 29.8 ± 20.5 mol/flash which is 59.4% larger than the basic one (18.7 ± 18.1 mol/flash). Meanwhile, LNO<sub>x</sub> PE (increasing from 54.5 ± 48.1 mol/flash to 88.5 ± 61.1 mol/flash) also depends on the configuration of LNO production in WRF-Chem. The comparison between Fig. 4 and Fig. 9 shows that LNO<sub>2</sub>Clean PE and LNO<sub>2</sub> PE are more similar while LNO<sub>2</sub> PE and NO<sub>2</sub>Vis PE present the same tendency. It remains unclear as to whether the NO-NO<sub>2</sub>-O<sub>3</sub> cycle or  
355 other LNO<sub>x</sub> reservoirs accounts for the increment of LNO<sub>x</sub> PE. This would need detailed source analysis in WRF-Chem and is beyond the scope of this study.

Figure 10 shows the average percentage changes in AMF<sub>LNO<sub>2</sub></sub>, AMF<sub>LNO<sub>x</sub></sub>, LNO<sub>2</sub> and LNO<sub>x</sub> between retrievals using profiles based on 1×200 mol NO flash<sup>-1</sup> and 2×500 mol NO flash<sup>-1</sup>. These results were obtained by averaging data over MJJA 2014 based on the method described in Sect. 2.5 with the criterion of CRF ≥ 90%. The effects on LNO<sub>2</sub> and LNO<sub>x</sub> retrieval from  
360 increasing LNO profile values show mostly the same tendency: smaller AMF<sub>LNO<sub>2</sub></sub> and AMF<sub>LNO<sub>x</sub></sub> leads to larger LNO<sub>2</sub> and LNO<sub>x</sub>, but the changes are regionally dependent. This is caused by the nonlinear calculation of AMF<sub>LNO<sub>2</sub></sub> and AMF<sub>LNO<sub>x</sub></sub>. As the contribution of LNO<sub>2</sub> increases, both the numerator and denominator of Eq. (2) increase. Note that the LNO<sub>2</sub> accounts for a fraction of NO<sub>2</sub> above the clouds, the magnitude of increasing denominator could be different than that of increasing numerator, resulting in a different effect on the AMF<sub>LNO<sub>2</sub></sub> and AMF<sub>LNO<sub>x</sub></sub>. As mentioned in Zhu et al. (2019), the lightning densities in the  
365 Southeast U.S. might be overestimated using the 2×500 mol NO flash<sup>-1</sup> setting and the same lightning parameterization as ours. Fortunately, the AMFs and estimated LNO<sub>2</sub> change little in that region. Because the Southeast U.S. has the highest flash density (Fig. 2), the NO<sub>2</sub> in the numerator of AMF is dominated by LNO<sub>2</sub>. Both the SCD and VCD will increase when the model uses higher LNO<sub>2</sub>. In other words, the sensitivity to the LNO setting decreases and the relative distribution of LNO<sub>2</sub> matters.

370 Figure 11 shows the comparison of the mean LNO and LNO<sub>2</sub> profiles in two specific regions where the 2×500 mol NO flash<sup>-1</sup> setting leads to lower and higher LNO<sub>2</sub> PEs, respectively. The first one (Fig. 11a) is the region (36°N – 37°N, 89°W – 90°W) containing the minimal negative percent change in LNO<sub>2</sub> (Fig. 10c). The second one (31°N – 32°N, 97°W – 98°W), Figure 11b, has the largest positive percent change in LNO<sub>2</sub> (Fig. 10c). Although the relative distributions of mean LNO and LNO<sub>2</sub> profiles are similar in both regions, the magnitude differs with a factor of 10. This phenomenon implies that the  
375 performance of lightning parameterization in WRF-Chem is regionally dependent and an unrealistic profile could appear in the UT. Although this sensitivity analysis is false in some regions, it allows the calculation of an upper limit on the NO<sub>2</sub> due to LNO and LNO<sub>2</sub> profiles. As discussed in Laughner and Cohen (2017), the scattering weights are uniform under cloudy

conditions and the sensitivity of  $\text{NO}_2$  is nearly constant with different pressure levels because of the high albedo. However, the relative distribution of  $\text{LNO}_2$  within the UT should be taken carefully into consideration. If the  $\text{LNO}_2/\text{NO}_2$  above the cloud is large enough (Fig. 11a), the  $\text{AMF}_{\text{LNO}_2}$  is largely determined by the ratio of  $\text{LNO}_2^{\text{Vis}}$  to  $\text{LNO}_2$  which is related to the relative distribution. When the condition of high  $\text{LNO}_2/\text{NO}_2$  is not met, both relative distribution and ratio are important (Fig. 11b).

To clarify this, we applied the same sensitivity test of different simulating LNO amounts for all four methods mentioned in Sect. 2.4:  $\text{LNO}_2$ ,  $\text{LNO}_2^{\text{Vis}}$ ,  $\text{LNO}_2^{\text{Clean}}$  and  $\text{NO}_2^{\text{Vis}}$  (Fig. 12). Note that the threshold for CRF is set to 100% to simplify Eq. (2) to Eq. (7). The overall differences of  $\text{LNO}_2^{\text{Clean}}$  and  $\text{NO}_2^{\text{Vis}}$  are smaller than those of  $\text{LNO}_2$  and  $\text{LNO}_2^{\text{Vis}}$ . Comparing the numerator and denominator in the equations, it is clear why the impact of different simulating LNO amounts is smaller in Fig. 12c and d. For  $\text{LNO}_2^{\text{Clean}}$  and  $\text{NO}_2^{\text{Vis}}$ , both the SCD and VCD will increase (decrease) when more (less)  $\text{LNO}_2$  or  $\text{NO}_2$  presents. The difference between Fig. 12a and Fig. 12b is the denominator: the total tropospheric  $\text{LNO}_2$  vertical column and visible  $\text{LNO}_2$  vertical column respectively. As a result, the negative values in Fig. 12a are caused by the part of  $\text{LNO}_2$  below the cloud. The uncertainty of retrieved  $\text{LNO}_2$  and  $\text{LNO}_x$  PEs is driven by this error, and we conservatively estimate this to be  $\pm 13\%$  and  $\pm 25\%$  respectively.

#### 4 Uncertainties Analysis

The uncertainties of the  $\text{LNO}_2$  and  $\text{LNO}_x$  PEs are estimated following Pickering et al. (2016), Allen et al. (2019), Bucsele et al. (2019), Laughner et al. (2019) and Lapierre et al. (2020). We determine the uncertainty due to BEHR tropopause pressure, cloud radiance fraction, cloud pressure, surface pressure, surface reflectivity, profile shape, profile location,  $V_{\text{strat}}$ , the detection efficiency of lightning,  $t_{\text{window}}$  and  $\text{LNO}_2$  lifetime numerically by perturbing each parameter in turn and re-retrieving the  $\text{LNO}_2$  and  $\text{LNO}_x$  with the perturbed values (Table 5).

The GEOS-5 monthly tropopause pressure, which is consistent with the NASA Standard Product, is applied instead of the variable WRF tropopause height to evaluate the uncertainty (6% for  $\text{LNO}_2$  PE and 4% for  $\text{LNO}_x$  PE) caused by the BEHR tropopause pressure. The cloud pressure bias is given as a function of cloud pressure and fraction by Acarreta et al. (2004) implying an uncertainty of 32%, the most likely uncertainty in the production analysis, for  $\text{LNO}_2$  PE and 34% for  $\text{LNO}_x$  PE. The resolution of GLOBE terrain height data is much higher than the OMI pixel and a fixed scale height is assumed in the BEHR algorithm. As a result, Laughner et al. (2019) compared the average WRF surface pressures to the GLOBE surface pressures and arrived at the largest bias of 1.5%. Based on the largest bias, we vary the surface pressure (limited to less than 1020 hPa) and the uncertainty can be neglected.

The error in cloud radiance fraction is transformed from cloud fraction using:

$$\sigma = 0.05 \cdot \left. \frac{\partial f_r}{\partial f_g} \right|_{f_{g,\text{pix}}} \quad (10)$$

where  $f_r$  is the cloud radiance fraction,  $f_g$  is the cloud fraction and  $f_{g,\text{pix}}$  is the cloud fraction of a specific pixel. We calculate  $\partial f_r / \partial f_g$  under  $f_{g,\text{pix}}$  by the relationship between all binned  $f_r$  and  $f_g$  with the increment of 0.05 for the each specific OMI

orbit. Considering the relationship, the error in cloud fraction is converted to an error in cloud radiance fraction of 2% for the  
410 LNO<sub>2</sub> and LNO<sub>x</sub> PEs.

The accuracy of the 500 m MODIS albedo product is usually within 5% of albedo observations at the validation sites and those exceptions with low quality flags have been found to be primarily within 10% of the field data (Schaaf et al., 2011). Since we use the bidirectional reflectance distribution function (BRDF) data directly, rather than including a radiative transfer model, 14% Lambertian equivalent reflectivity (LER) error and 10% uncertainty are combined to get a perturbation of 17% (Laughner  
415 et al., 2019). The uncertainty due to surface reflectivity can be neglected with the 17% perturbation.

As discussed at the end of Sect. 3.4, another setting of LNO<sub>2</sub> ( $2 \times 500 \text{ mol NO flash}^{-1}$ ) is applied to determine the uncertainty of the lightning parameterization and the vertical distribution of LNO in WRF-Chem. Differences between the two profiles lead to an uncertainty of 13% and 25% in the resulting PEs of LNO<sub>2</sub> and LNO<sub>x</sub>. Another sensitivity test allows each pixel to shift by -0.2, 0, or +0.2 degrees in the directions of longitude and latitude, taking advantage of the high-resolution profile location  
420 in WRF-Chem. The resulting uncertainty of LNO<sub>x</sub> PE is 1% including the error of transport and chemistry by shifting pixels.

Compared to the NASA standard product v2, Krotkov et al. (2017) demonstrated that the noise in  $V_{\text{strat}}$  is  $1 \times 10^{14} \text{ cm}^{-2}$ . Errors in polluted regions can be slightly larger than this value, while errors in the cleanest areas are typically significantly smaller (Bucsela et al., 2013). We estimated the uncertainty of  $V_{\text{strat}}$  component and the slant column errors to be 10% and 5%, respectively, following Allen et al. (2019).

425 Based on the standard deviation of the detection efficiency estimation over the CONUS relative to LIS, ENTLN detection efficiency uncertainties are  $\pm 16\%$  for total and IC flashes/strokes. Due to the high detection efficiency of CG over the CONUS, the uncertainty is estimated to be  $\pm 5\%$  (Lapierre et al., 2020). It is found that the resulting uncertainty of detection efficiency is 15% in the production analysis. We have used the  $t_{\text{window}}$  of 2.4 h for counting ENTLN flashes and strokes to analyze LNO<sub>2</sub> and LNO<sub>x</sub> production. Because  $t_{\text{window}}$  derived from the ERA5 reanalysis can not represent the variable wind speeds, a sensitivity  
430 test is performed which yields an uncertainty of 10% for production per flash and 8% for production per stroke using  $t_{\text{window}}$  of 2 h and 4 h. Meanwhile, the lifetime of UT NO<sub>x</sub> ranges from 2 hours to 12 hours depending on the convective location, the methyl peroxy nitrate and alkyl and multifunctional nitrates (Nault et al., 2017). The lifetime ( $\tau$ ) of NO<sub>2</sub> in Eq. (6) is replaced by 2 and 12 hours to determine the uncertainty as 24% due to lifetime. This is comparable with the uncertainty (25%) caused by lightning parameterization for the LNO<sub>x</sub> type.

435 Recent works revealed that the modeled NO/NO<sub>2</sub> ratio departs from the data in the SEAC<sup>4</sup>RS aircraft campaign (Travis et al., 2016; Silvern et al., 2018). Silvern et al. (2018) attributed this to the positive interference on the NO<sub>2</sub> measurements or errors in the cold-temperature NO-NO<sub>2</sub>-O<sub>3</sub> photochemical reaction rate. We assign a 20% bias with  $\pm 15\%$  uncertainty to this error considering the possible positive NO<sub>2</sub> measurements interferences (Allen et al., 2019; Bucsela et al., 2019) and estimate the uncertainty to be 15% for LNO<sub>x</sub> PE.

440 In addition, the estimation of LNO<sub>x</sub> PE also depends on the tropospheric background NO<sub>2</sub>. In our method, main factors affecting this factor are the emissions inventory and the amount of transported NO<sub>2</sub>. For the emissions inventory, the sources of uncertainty are assumptions, methods, input data and calculation errors. As a result, the uncertainties for different species or pollutants related to NO<sub>2</sub> are different and EPA also doesn't publish the quantified uncertainty measures because the parties

that submit emissions estimates to EPA are not asked to include quantitative uncertainty measurements or estimates (EPA, 445 2015). For the simulated convective transport, Li et al. (2018) compared the cloud-resolving simulations with these based on convective parameterization and pointed out that the convective transport was weaker in the parameterization. But, we believe that the ratio condition ( $\text{LNO}_2^{\text{Vis}}/\text{NO}_2^{\text{Vis}} \geq 50\%$ ) should reduce these two kinds of uncertainty and assume an uncertainty of 10%, which is less than 20% assigned in Allen et al. (2019) and Bucselá et al. (2019).

The overall uncertainty is estimated as the square root of the sum of the squares of all individual uncertainties in Table 450 5. The net uncertainty is 48% and 56% for  $\text{LNO}_2$  type and  $\text{LNO}_x$  type respectively. The mean  $\text{LNO}_2/\text{flash}$ ,  $\text{LNO}_x/\text{flash}$ ,  $\text{LNO}_2/\text{stroke}$ ,  $\text{LNO}_x/\text{stroke}$  based on the linear regression and summation method are 32 mol/flash, 90 mol/flash, 6 mol/stroke and 17 mol/stroke. Applying the corresponding uncertainty to these mean values, we arrive at  $32 \pm 15$  mol  $\text{LNO}_2/\text{flash}$ ,  $90 \pm 50$  mol  $\text{LNO}_x/\text{flash}$ ,  $6 \pm 3$  mol  $\text{LNO}_2/\text{stroke}$  and  $17 \pm 10$  mol  $\text{LNO}_x/\text{stroke}$ . This is in the range of current literature estimate ranging from 33 to 500 mol  $\text{LNO}_x/\text{flash}$  (Schumann and Huntrieser, 2007; Beirle et al., 2010; Bucselá et al., 2010). Bucselá 455 et al. (2010) estimated  $\text{LNO}_x$  PE of 100 – 250 mol/flash which is higher than but overlaps with our estimate. Pickering et al. (2016) estimated  $\text{LNO}_x$  PE to be  $80 \pm 45$  mol per flash for the Gulf of Mexico. This is 50% smaller than our flash-based results over the CONUS, if we use the same linear regression method which is based on the daily summed values instead of daily mean values. Note that the criteria defined in Sect. 3.1 lead to many missing data over the Gulf of Mexico, thus it is actually a comparison between different regions. For the stroke-based results, Lapierre et al. (2020) yields lower  $\text{LNO}_2$  PE of  $1.6 \pm 0.1$  460 mol per stroke, the difference is caused by the different version of BEHR algorithm and several settings as mentioned in Sect. 3.2. Bucselá et al. (2019) inferred an average value of  $200 \pm 110$  moles (122% larger than our results)  $\text{LNO}_x$  produced per flash over the North America, this is related to the different algorithm, lightning data and lightning thresholds.

## 5 Conclusions

In this study, a new algorithm for retrieving  $\text{LNO}_2$  ( $\text{LNO}_x$ ) from OMI, including  $\text{LNO}_2$  ( $\text{LNO}_x$ ) below cloud, has been de- 465 veloped for application over active convection. It works in both clean and polluted regions because of the consideration of tropospheric background pollution in the definition of AMFs. It uses specific criteria combining with several other conditions (sufficient CRF, coincident ENTLN data,  $\text{TL} \geq 1000$  and ratio  $\geq 50\%$ ) to ensure that the electrically active regions are detected by OMI and simulated by WRF-Chem successfully. We conducted an analysis on  $1^\circ \times 1^\circ$  daily boxes in MJJA 2014 and obtained the seasonal mean  $\text{LNO}_2$  and  $\text{LNO}_x$  production efficiencies over the CONUS. Considering all the uncertainties 470 (Table 5) and applying the summation and regression method, the final mean production efficiencies are estimated to be  $32 \pm 15$  mol  $\text{LNO}_2/\text{flash}$ ,  $90 \pm 50$  mol  $\text{LNO}_x/\text{flash}$ ,  $6 \pm 3$  mol  $\text{LNO}_2/\text{stroke}$  and  $17 \pm 10$  mol  $\text{LNO}_x/\text{stroke}$ .

Compared with Lapierre et al. (2020), we find that the  $\text{LNO}_2$  production could be larger when the below-cloud  $\text{LNO}_2$  is taken into account, especially for the high clouds. Meanwhile, if the method of Pickering et al. (2016) is applied without the background  $\text{NO}_2$  correction, the derived  $\text{LNO}_x$  production efficiency is similar to ours in clean regions or regions with high 475  $\text{LNO}_2$  concentration above the cloud, but it could be overestimated more than 18% in polluted regions. Finally, implementing profiles generated with different model settings of lightning ( $1 \times 200$  mol NO flash $^{-1}$  and  $2 \times 500$  mol NO flash $^{-1}$ ), we find that

the larger LNO production setting leads to 62% larger retrieval of LNO<sub>x</sub> on average despite some regionally dependent effects caused by the nonlinear calculation of AMF. Both the ratio of the tropospheric LNO<sub>2</sub> above the cloud to the total tropospheric LNO<sub>2</sub> and the ratio of LNO<sub>2</sub> to NO<sub>2</sub> cause different comprehensive effects due to the nonlinear calculation of AMF<sub>LNO<sub>2</sub></sub> and AMF<sub>LNO<sub>x</sub></sub>.

Since other regions, like China and India, have much more NO<sub>2</sub> pollution than the CONUS, it is necessary to consider the background NO<sub>2</sub> in detail. These analyses will be complemented by the recently launched satellite instrument (TROPOspheric Monitoring Instrument [TROPOMI]) (Veefkind et al., 2012; Boersma et al., 2018; Griffin et al., 2019) and Lightning Mapping Imager (LMI) on the new generation Chinese geostationary meteorological satellites Fengyun-4 (Min et al., 2017; Yang et al., 2017; Zhang et al., 2019). Future work investigating the flash channel length and more detailed lightning parameterization in WRF-Chem would greatly benefit LNO<sub>x</sub> estimation. Applying current method in future studies may enhance the accuracy of LNO<sub>x</sub> production at both local and global scales.

*Code and data availability.* The retrieval algorithm used in Sect. 2.4 is available at <https://github.com/zxdawn/BEHR-LNOx> (last access: March 8, 2020; Zhang and Laughner, 2019). The WRF-Chem model output and LNO<sub>x</sub> product are available upon request to Xin Zhang (xinzhang1215@gmail.com).

#### Appendix A: AMF Definitions used in this Study

$$AMF_{LNO_2} = \frac{(1 - f_r) \int_{p_{surf}}^{p_{tp}} w_{clear}(p) NO_2(p) dp + f_r \int_{p_{cloud}}^{p_{tp}} w_{cloudy}(p) NO_2(p) dp}{\int_{p_{surf}}^{p_{tp}} LNO_2(p) dp} \quad (A1)$$

$$AMF_{LNO_x} = \frac{(1 - f_r) \int_{p_{surf}}^{p_{tp}} w_{clear}(p) NO_2(p) dp + f_r \int_{p_{cloud}}^{p_{tp}} w_{cloudy}(p) NO_2(p) dp}{\int_{p_{surf}}^{p_{tp}} LNO_x(p) dp} \quad (A2)$$

where  $f_r$  is the cloud radiance fraction,  $p_{surf}$  is the surface pressure,  $p_{tp}$  is the tropopause pressure,  $p_{cloud}$  is the cloud optical pressure (CP),  $w_{clear}$  and  $w_{cloudy}$  are respectively the pressure dependent scattering weights from the TOMRAD lookup table (Bucsela et al., 2013) for clear and cloudy parts, and  $NO_2(p)$  is the modeled NO<sub>2</sub> vertical profile.  $LNO_2(p)$  and  $LNO_x(p)$  are respectively the LNO<sub>2</sub> and LNO<sub>x</sub> vertical profile calculated by the difference of vertical profiles between WRF-Chem simulations with and without lightning.

$$AMF_{LNO_2Clean} = \frac{(1 - f_r) \int_{p_{surf}}^{p_{tp}} w_{clear}(p) LNO_2(p) dp + f_r \int_{p_{cloud}}^{p_{tp}} w_{cloudy}(p) LNO_2(p) dp}{\int_{p_{surf}}^{p_{tp}} LNO_2(p) dp} \quad (A3)$$

$$AMF_{NO_2Vis} = \frac{(1 - f_r) \int_{p_{surf}}^{p_{tp}} w_{clear}(p) NO_2(p) dp + f_r \int_{p_{cloud}}^{p_{tp}} w_{cloudy}(p) NO_2(p) dp}{(1 - f_g) \int_{p_{surf}}^{p_{tp}} NO_2(p) dp + f_g \int_{p_{cloud}}^{p_{tp}} NO_2(p) dp} \quad (A4)$$



$$AMF_{NO_x \text{ Vis}} = \frac{(1 - f_r) \int_{p_{\text{surf}}}^{p_{\text{tp}}} w_{\text{clear}}(p) NO_2(p) dp + f_r \int_{p_{\text{cloud}}}^{p_{\text{tp}}} w_{\text{cloudy}}(p) NO_2(p) dp}{(1 - f_g) \int_{p_{\text{surf}}}^{p_{\text{tp}}} NO_x(p) dp + f_g \int_{p_{\text{cloud}}}^{p_{\text{tp}}} NO_x(p) dp} \quad (\text{A5})$$

$$AMF_{LNO_2 \text{ Vis}} = \frac{(1 - f_r) \int_{p_{\text{surf}}}^{p_{\text{tp}}} w_{\text{clear}}(p) NO_2(p) dp + f_r \int_{p_{\text{cloud}}}^{p_{\text{tp}}} w_{\text{cloudy}}(p) NO_2(p) dp}{(1 - f_g) \int_{p_{\text{surf}}}^{p_{\text{tp}}} LNO_2(p) dp + f_g \int_{p_{\text{cloud}}}^{p_{\text{tp}}} LNO_2(p) dp} \quad (\text{A6})$$

where  $f_g$  is the geometric cloud fraction and  $NO_x(p)$  is the modeled  $NO_x$  vertical profile.

## Appendix B: LNO<sub>x</sub> Production based on Lower Lightning Thresholds

505 While we used 2400 flashes  $\text{box}^{-1}$  and 8160 strokes  $\text{box}^{-1}$  per 2.4 hour time window for detecting LNO<sub>x</sub>, here we show results obtained when using 1 flash  $\text{box}^{-1}$  and 3.4 strokes  $\text{box}^{-1}$  in the same time window. We note that the WRF total lightning threshold is also reduced to 1 flash  $\text{box}^{-1}$ , but we keep the ratio condition unchanged. Briefly, the condition is CRF90\_ENTLN1(3.4)\_TL1\_ratio50 as shown in Table 1.

Similarly, the order of estimated daily PEs is LNO<sub>2</sub>Clean > LNO<sub>2</sub> > NO<sub>2</sub>Vis > LNO<sub>2</sub>Vis (Fig. B1). Compared with Fig. 4,  
510 the LNO<sub>2</sub> per flash and LNO<sub>x</sub> per flash are larger while PEs based on stroke data are smaller. Considering the additional boxes of fewer lightning counts, differences in the daily mean flashes and NO<sub>x</sub> results in different PEs and the relationship presents more like the power function as mentioned in Bucsela et al. (2019).

Instead of using the nonlinear regression of power function:

$$y = \alpha x^\beta \quad (\text{B1})$$

515 where  $x$  is flashes or strokes and  $y$  is NO<sub>2</sub> or NO<sub>x</sub>, we take the logarithm of both sides and apply the linear regression to data:

$$\log_{10} y = \log_{10} \alpha + \beta \log_{10} x \quad (\text{B2})$$

As expected, the linear regression based on logarithmized data performs better in this situation and yields  $\alpha = 38 \text{ kmol}$ , and  $\beta = 0.3$  for LNO<sub>x</sub> per flash (Fig. B2). Since we use the unbinned data (flashes not divided into many groups), we compare our results with Bucsela et al. (2019) based on the same kind of data ( $\alpha = 10.3 \text{ kmol}$ , and  $\beta = 0.42$ ). The large difference of  $\alpha$   
520 is related to the method of estimating LNO<sub>x</sub>, different lightning data (WWLLN and ENTLN) and different regions (northern midlatitudes and CONUS). Note that the resolution ( $13 \times 24 \text{ km}^2$ ) of OMI could weaken the signal of LNO<sub>x</sub>. We believe the phenomenon of higher production efficiency as flash rate decreases (Fig. B3) could be explored in much detail with higher resolution data like the TROPOMI data.

*Author contributions.* YY directed the research and RJvdA, XZ and YY designed the research with feedback from the other co-authors;  
525 RJvdA and XZ developed the algorithm; JLL provided guidance and supporting data on the ENTLN data; XZ performed simulations and

analysis with the help of YY, RJvdA, QC, XK, SY, JC, CH and RS; YY, RJvdA, JLL and XZ interpreted the data and discussed the results. XZ drafted the manuscript with comments from the co-authors; JLL, RJvdA and YY edited the manuscript.

*Competing interests.* The authors declare that they have no conflict of interest.

*Acknowledgements.* This work was funded by the National Natural Science Foundation of China (91644224 and 41705118). We acknowledge use of the computational resource provided by the National Supercomputer Centre in Guangzhou (NSCC-GZ). We thank the University of California Berkeley Satellite Group for the basic BEHR algorithm. We also thank Earth Networks Company for providing the Earth Networks Total Lightning Network (ENTLN) datasets. We appreciate the discussions with Joshua L. Laughner for BEHR codes and Mary Barth for the WRF-Chem lightning NO<sub>x</sub> module. MOZART-4 global model output is available at <https://www.acom.ucar.edu/wrf-chem/mozart.shtml> (last access: March 8, 2020). The authors would also like to thank all anonymous reviewers as well as Kenneth E. Pickering, Eric J. Bucsela and Dale J. Allen for detailed comments which greatly improved this manuscript. Finally, we thank all contributors of Python packages used in this paper (Met Office, 2010 - 2015; Hoyer and Hamman, 2017; Hunter, 2007; Jiawei Zhuang et al., 2019; McKinney, 2011; Inc., 2015; Seabold and Perktold, 2010; van der Walt et al., 2011; Waskom et al., 2017).

## References

- 540 Acarreta, J. R., de Haan, J. F., and Stammes, P.: Cloud pressure retrieval using the O<sub>2</sub> -O<sub>2</sub> absorption band at 477 nm, *Journal of Geophysical Research*, 109, 2165, <https://doi.org/10.1029/2003JD003915>, 2004.
- Allen, D. J., Pickering, K. E., Duncan, B. N., and Damon, M.: Impact of lightning NO emissions on North American photochemistry as determined using the Global Modeling Initiative (GMI) model, *Journal of Geophysical Research*, 115, 4711, <https://doi.org/10.1029/2010JD014062>, 2010.
- 545 Allen, D. J., Pickering, K. E., Pinder, R. W., Henderson, B. H., Appel, K. W., and Prados, A.: Impact of lightning-NO on eastern United States photochemistry during the summer of 2006 as determined using the CMAQ model, *Atmospheric Chemistry and Physics*, 12, 1737–1758, <https://doi.org/10.5194/acp-12-1737-2012>, 2012.
- Allen, D. J., Pickering, K. E., Bucseła, E. J., Krotkov, N., and Holzworth, R.: Lightning NO<sub>x</sub> Production in the Tropics as Determined Using OMI NO<sub>2</sub> Retrievals and WLLN Stroke Data, *Journal of Geophysical Research: Atmospheres*, <https://doi.org/10.1029/2018JD029824>, 2019.
- 550 Banerjee, A., Archibald, A. T., Maycock, A. C., Telford, P., Abraham, N. L., Yang, X., Braesicke, P., and Pyle, J. A.: Lightning NO<sub>x</sub>, a key chemistry–climate interaction: impacts of future climate change and consequences for tropospheric oxidising capacity, *Atmospheric Chemistry and Physics*, 14, 9871–9881, <https://doi.org/10.5194/acp-14-9871-2014>, 2014.
- Barth, M. C., Lee, J., Hodzic, A., Pfister, G., Skamarock, W. C., Worden, J., Wong, J., and Noone, D.: Thunderstorms and upper troposphere chemistry during the early stages of the 2006 North American Monsoon, *Atmospheric Chemistry and Physics*, 12, 11 003–11 026, <https://doi.org/10.5194/acp-12-11003-2012>, 2012.
- 555 Beirle, S., Platt, U., Wenig, M., and Wagner, T.: NO<sub>x</sub> production by lightning estimated with GOME, *Advances in Space Research*, 34, 793–797, <https://doi.org/10.1016/j.asr.2003.07.069>, 2004.
- Beirle, S., Spichtinger, N., Stohl, A., Cummins, K. L., Turner, T., Boccippio, D., Cooper, O. R., Wenig, M., Grzegorski, M., Platt, U., and Wagner, T.: Estimating the NO<sub>x</sub> produced by lightning from GOME and NLDN data: A case study in the Gulf of Mexico, *Atmospheric Chemistry and Physics*, 6, 1075–1089, <https://doi.org/10.5194/acp-6-1075-2006>, 2006.
- 560 Beirle, S., Salzmann, M., Lawrence, M. G., and Wagner, T.: Sensitivity of satellite observations for freshly produced lightning NO<sub>x</sub>, *Atmospheric Chemistry and Physics*, 9, 1077–1094, <https://doi.org/10.5194/acp-9-1077-2009>, 2009.
- Beirle, S., Huntrieser, H., and Wagner, T.: Direct satellite observation of lightning-produced NO<sub>x</sub>, *Atmospheric Chemistry and Physics*, 10, 10965–10986, <https://doi.org/10.5194/acp-10-10965-2010>, 2010.
- 565 Bela, M. M., Barth, M. C., Toon, O. B., Fried, A., Homeyer, C. R., Morrison, H., Cummings, K. A., Li, Y., Pickering, K. E., Allen, D. J., Yang, Q., Wennberg, P. O., Crouse, J. D., St. Clair, J. M., Teng, A. P., O’Sullivan, D., Huey, L. G., Chen, D., Liu, X., Blake, D. R., Blake, N. J., Apel, E. C., Hornbrook, R. S., Flocke, F., Campos, T., and Diskin, G.: Wet scavenging of soluble gases in DC3 deep convective storms using WRF-Chem simulations and aircraft observations, *Journal of Geophysical Research: Atmospheres*, 121, 4233–4257, <https://doi.org/10.1002/2015JD024623>, 2016.
- 570 Boersma, K. F., Eskes, H. J., Meijer, E. W., and Kelder, H. M.: Estimates of lightning NO<sub>x</sub> production from GOME satellite observations, *Atmospheric Chemistry and Physics*, 5, 2311–2331, <https://doi.org/10.5194/acp-5-2311-2005>, 2005.
- Boersma, K. F., Eskes, H. J., Richter, A., de Smedt, I., Lorente, A., Beirle, S., van Geffen, J. H. G. M., Zara, M., Peters, E., van Roozendaal, M., Wagner, T., de Maasackers, J., van der A, R. J., Nightingale, J., de Rudder, A., Irie, H., Pinardi, G., Lambert, J.-C., and Compernelle, S. C.: Improving algorithms and uncertainty estimates for satellite NO<sub>2</sub> retrievals: results from the quality assurance for the essential

- 575 climate variables (QA4ECV) project, *Atmospheric Measurement Techniques*, 11, 6651–6678, <https://doi.org/10.5194/amt-11-6651-2018>, 2018.
- Bovensmann, H., Burrows, J. P., Buchwitz, M., Frerick, J., Noël, S., Rozanov, V. V., Chance, K. V., and Goede, A. P. H.: SCIAMACHY: Mission Objectives and Measurement Modes, *Journal of the Atmospheric Sciences*, 56, 127–150, [https://doi.org/10.1175/1520-0469\(1999\)056<0127:SMOAMM>2.0.CO;2](https://doi.org/10.1175/1520-0469(1999)056<0127:SMOAMM>2.0.CO;2), 1999.
- 580 Browne, E. C., Wooldridge, P. J., Min, K.-E., and Cohen, R. C.: On the role of monoterpene chemistry in the remote continental boundary layer, *Atmospheric Chemistry and Physics*, 14, 1225–1238, <https://doi.org/10.5194/acp-14-1225-2014>, 2014.
- Bucsela, E. J., Pickering, K. E., Huntemann, T. L., Cohen, R. C., Perring, A., Gleason, J. F., Blakeslee, R. J., Albrecht, R. I., Holzworth, R., Cipriani, J. P., Vargas-Navarro, D., Mora-Segura, I., Pacheco-Hernández, A., and Laporte-Molina, S.: Lightning-generated NO<sub>x</sub> seen by the Ozone Monitoring Instrument during NASA's Tropical Composition, Cloud and Climate Coupling Experiment (TC<sup>4</sup>), *Journal of Geophysical Research*, 115, 793, <https://doi.org/10.1029/2009JD013118>, 2010.
- 585 Bucsela, E. J., Krotkov, N. A., Celarier, E. A., Lamsal, L. N., Swartz, W. H., Bhartia, P. K., Boersma, K. F., Veefkind, J. P., Gleason, J. F., and Pickering, K. E.: A new stratospheric and tropospheric NO<sub>2</sub> retrieval algorithm for nadir-viewing satellite instruments: Applications to OMI, *Atmospheric Measurement Techniques*, 6, 2607–2626, <https://doi.org/10.5194/amt-6-2607-2013>, 2013.
- Bucsela, E. J., Pickering, K. E., Allen, D. J., Holzworth, R., and Krotkov, N. A.: Midlatitude lightning NO<sub>x</sub> production efficiency inferred from OMI and WLLN data, *Journal of Geophysical Research: Atmospheres*, <https://doi.org/10.1029/2019JD030561>, 2019.
- 590 Burrows, J. P., Weber, M., Buchwitz, M., Rozanov, V., Ladstätter-Weissenmayer, A., Richter, A., DeBeek, R., Hoogen, R., Bramstedt, K., Eichmann, K.-U., Eisinger, M., and Perner, D.: The Global Ozone Monitoring Experiment (GOME): Mission Concept and First Scientific Results, *Journal of the Atmospheric Sciences*, 56, 151–175, [https://doi.org/10.1175/1520-0469\(1999\)056<0151:TGOMEG>2.0.CO;2](https://doi.org/10.1175/1520-0469(1999)056<0151:TGOMEG>2.0.CO;2), 1999.
- Callies, J., Corpaccioli, E., Eisinger, M., Hahne, A., and Lefebvre, A.: GOME-2-Metop's second-generation sensor for operational ozone monitoring, *ESA bulletin*, 102, 28–36, 2000.
- 595 Carey, L. D., Koshak, W., Peterson, H., and Mecikalski, R. M.: The kinematic and microphysical control of lightning rate, extent, and NO<sub>x</sub> production, *Journal of Geophysical Research: Atmospheres*, 121, 7975–7989, <https://doi.org/10.1002/2015JD024703>, 2016.
- Choi, S., Joiner, J., Choi, Y., Duncan, B. N., Vasilkov, A., Krotkov, N., and Bucsela, E.: First estimates of global free-tropospheric NO<sub>2</sub> abundances derived using a cloud-slicing technique applied to satellite observations from the Aura Ozone Monitoring Instrument (OMI), *Atmospheric Chemistry and Physics*, 14, 10 565–10 588, <https://doi.org/10.5194/acp-14-10565-2014>, 2014.
- 600 Clark, S. K., Ward, D. S., and Mahowald, N. M.: Parameterization-based uncertainty in future lightning flash density, *Geophysical Research Letters*, 44, 2893–2901, <https://doi.org/10.1002/2017GL073017>, 2017.
- Davis, T. C., Rutledge, S. A., and Fuchs, B. R.: Lightning location, NO<sub>x</sub> production, and transport by anomalous and normal polarity thunderstorms, *Journal of Geophysical Research: Atmospheres*, <https://doi.org/10.1029/2018JD029979>, 2019.
- 605 DeCaria, A. J., Pickering, K. E., Stenichikov, G. L., Scala, J. R., Stith, J. L., Dye, J. E., Ridley, B. A., and Laroche, P.: A cloud-scale model study of lightning-generated NO<sub>x</sub> in an individual thunderstorm during STERAO-A, *Journal of Geophysical Research*, 105, 11 601–11 616, <https://doi.org/10.1029/2000JD900033>, 2000.
- DeCaria, A. J., Pickering, K. E., Stenichikov, G. L., and Ott, L. E.: Lightning-generated NO<sub>x</sub> and its impact on tropospheric ozone production: A three-dimensional modeling study of a Stratosphere-Troposphere Experiment: Radiation, Aerosols and Ozone (STERAO-A) thunderstorm, *Journal of Geophysical Research*, 110, n/a–n/a, <https://doi.org/10.1029/2004JD005556>, 2005.
- 610

- Dobber, M., Kleipool, Q., Dirksen, R., Levelt, P., Jaross, G., Taylor, S., Kelly, T., Flynn, L., Leppelmeier, G., and Rozemeijer, N.: Validation of Ozone Monitoring Instrument level 1b data products, *Journal of Geophysical Research*, 113, 5224, <https://doi.org/10.1029/2007JD008665>, 2008.
- Emmons, L. K., Walters, S., Hess, P. G., Lamarque, J.-F., Pfister, G. G., Fillmore, D., Granier, C., Guenther, A., Kinnison, D., Laepple, T.,  
615 Orlando, J., Tie, X., Tyndall, G., Wiedinmyer, C., Baughcum, S. L., and Kloster, S.: Description and evaluation of the Model for Ozone and Related chemical Tracers, version 4 (MOZART-4), *Geoscientific Model Development*, 3, 43–67, <https://doi.org/10.5194/gmd-3-43-2010>, 2010.
- EPA, U.: 2011 National Emissions Inventory, version 2—Technical support document, US Environmental Protection Agency, Office of Air Quality Planning and Standards. Accessed August 2017., 2015.
- 620 EPA, U. S. and OAR: Air Pollutant Emissions Trends Data | US EPA, <https://www.epa.gov/air-emissions-inventories/air-pollutant-emissions-trends-data>, 2015.
- Finney, D. L., Doherty, R. M., Wild, O., Young, P. J., and Butler, A.: Response of lightning NO<sub>x</sub> emissions and ozone production to climate change: Insights from the Atmospheric Chemistry and Climate Model Intercomparison Project, *Geophysical Research Letters*, 43, 5492–5500, <https://doi.org/10.1002/2016GL068825>, 2016.
- 625 Finney, D. L., Doherty, R. M., Wild, O., Stevenson, D. S., MacKenzie, I. A., and Blyth, A. M.: A projected decrease in lightning under climate change, *Nature Climate Change*, 8, 210–213, <https://doi.org/10.1038/s41558-018-0072-6>, 2018.
- Fried, A., Barth, M. C., Bela, M., Weibring, P., Richter, D., Walega, J., Li, Y., Pickering, K., Apel, E., Hornbrook, R., Hills, A., Riemer, D. D., Blake, N., Blake, D. R., Schroeder, J. R., Luo, Z. J., Crawford, J. H., Olson, J., Rutledge, S., Betten, D., Biggerstaff, M. I., Diskin, G. S., Sachse, G., Campos, T., Flocke, F., Weinheimer, A., Cantrell, C., Pollack, I., Peischl, J., Froyd, K., Wisthaler, A., Mikoviny,  
630 T., and Woods, S.: Convective transport of formaldehyde to the upper troposphere and lower stratosphere and associated scavenging in thunderstorms over the central United States during the 2012 DC3 study, *Journal of Geophysical Research: Atmospheres*, 121, 7430–7460, <https://doi.org/10.1002/2015JD024477>, 2016.
- Fuchs, B. R. and Rutledge, S. A.: Investigation of Lightning Flash Locations in Isolated Convection Using LMA Observations, *Journal of Geophysical Research: Atmospheres*, 123, 6158–6174, <https://doi.org/10.1002/2017JD027569>, 2018.
- 635 Goliff, W. S., Stockwell, W. R., and Lawson, C. V.: The regional atmospheric chemistry mechanism, version 2, *Atmospheric Environment*, 68, 174–185, <https://doi.org/10.1016/j.atmosenv.2012.11.038>, 2013.
- Grell, G. A., Peckham, S. E., Schmitz, R., McKeen, S. A., Frost, G., Skamarock, W. C., and Eder, B.: Fully coupled “online” chemistry within the WRF model, *Atmospheric Environment*, 39, 6957–6975, <https://doi.org/10.1016/j.atmosenv.2005.04.027>, 2005.
- Griffin, D., Zhao, X., McLinden, C. A., Boersma, F., Bourassa, A., Dammers, E., Degenstein, D., Eskes, H., Fehr, L., Fioletov, V., Hayden,  
640 K., Kharol, S. K., Li, S.-M., Makar, P., Martin, R. V., Mihele, C., Mittermeier, R. L., Krotkov, N., Snee, M., Lamsal, L. N., Linden, M. t., van Geffen, J., Veefkind, P., and Wolde, M.: High-Resolution Mapping of Nitrogen Dioxide With TROPOMI: First Results and Validation Over the Canadian Oil Sands, *Geophysical Research Letters*, 46, 1049–1060, <https://doi.org/10.1029/2018GL081095>, 2019.
- Guenther, A., Karl, T., Harley, P., Wiedinmyer, C., Palmer, P. I., and Geron, C.: Estimates of global terrestrial isoprene emissions using MEGAN (Model of Emissions of Gases and Aerosols from Nature), *Atmospheric Chemistry and Physics*, 6, 3181–3210, <https://hal.archives-ouvertes.fr/hal-00295995>, 2006.
- 645 Hauglustaine, D., Emmons, L., Newchurch, M., Brasseur, G., Takao, T., Matsubara, K., Johnson, J., Ridley, B., Stith, J., and Dye, J.: On the Role of Lightning NO<sub>x</sub> in the Formation of Tropospheric Ozone Plumes: A Global Model Perspective, *Journal of Atmospheric Chemistry*, 38, 277–294, <https://doi.org/10.1023/A:1006452309388>, 2001.

- Hoyer, S. and Hamman, J.: xarray: N-D labeled arrays and datasets in Python, *Journal of Open Research Software*, 5, <https://doi.org/10.5334/jors.148>, <http://doi.org/10.5334/jors.148>, 2017.
- 650 Hunter, J. D.: Matplotlib: A 2D Graphics Environment, *Computing in Science & Engineering*, 9, 90–95, <https://doi.org/10.1109/MCSE.2007.55>, 2007.
- Inc., P. T.: Collaborative data science, <https://plot.ly>, 2015.
- Jiawei Zhuang, Jiling, A., and Rasp, S.: JiaweiZhuang/xESMF: v0.2.1, <https://doi.org/10.5281/zenodo.1134365>, 2019.
- 655 Joiner, J., Vasilkov, A. P., Gupta, P., Bhartia, P. K., Veefkind, P., Sneep, M., de Haan, J., Polonsky, I., and Spurr, R.: Fast simulators for satellite cloud optical centroid pressure retrievals; evaluation of OMI cloud retrievals, *Atmospheric Measurement Techniques*, 5, 529–545, <https://doi.org/10.5194/amt-5-529-2012>, 2012.
- KNMI: Background information about the Row Anomaly in OMI, <http://projects.knmi.nl/omi/research/product/rowanomaly-background.php>, last access: March 8, 2020, 2012.
- 660 Krause, A., Kloster, S., Wilkenskjeld, S., and Paeth, H.: The sensitivity of global wildfires to simulated past, present, and future lightning frequency, *Journal of Geophysical Research: Biogeosciences*, 119, 312–322, <https://doi.org/10.1002/2013JG002502>, 2014.
- Krotkov, N. A., Lamsal, L. N., Celarier, E. A., Swartz, W. H., Marchenko, S. V., Bucsela, E. J., Chan, K. L., Wenig, M., and Zara, M.: The version 3 OMI NO<sub>2</sub> standard product, *Atmospheric Measurement Techniques*, 10, 3133–3149, <https://doi.org/10.5194/amt-10-3133-2017>, 2017.
- 665 Kuhlmann, G., Hartl, A., Cheung, H. M., Lam, Y. F., and Wenig, M. O.: A novel gridding algorithm to create regional trace gas maps from satellite observations, *Atmospheric Measurement Techniques*, 7, 451–467, <https://doi.org/10.5194/amt-7-451-2014>, 2014.
- Lapierre, J. L., Laughner, J. L., Geddes, J. A., Koshak, W., Cohen, R. C., and Pusede, S. E.: Observing U.S. regional variability in lightning NO<sub>2</sub> production rates, *Journal of Geophysical Research: Atmospheres*, <https://doi.org/10.1029/2019JD031362>, 2020.
- Laughner, J. L. and Cohen, R. C.: Quantification of the effect of modeled lightning NO<sub>2</sub> on UV–visible air mass factors, *Atmospheric*
- 670 *Measurement Techniques*, 10, 4403–4419, <https://doi.org/10.5194/amt-10-4403-2017>, 2017.
- Laughner, J. L., Zhu, Q., and Cohen, R. C.: The Berkeley High Resolution Tropospheric NO<sub>2</sub> Product, *Earth System Science Data Discussions*, pp. 1–33, <https://doi.org/10.5194/essd-2018-66>, 2018a.
- Laughner, J. L., Zhu, Q., and Cohen, R. C.: Evaluation of version 3.0B of the BEHR OMI NO<sub>2</sub> product, *Atmospheric Measurement Techniques Discussions*, pp. 1–25, <https://doi.org/10.5194/amt-2018-248>, 2018b.
- 675 Laughner, J. L., Zhu, Q., and Cohen, R. C.: Evaluation of version 3.0B of the BEHR OMI NO<sub>2</sub> product, *Atmospheric Measurement Techniques*, 12, 129–146, <https://doi.org/10.5194/amt-12-129-2019>, 2019.
- Levelt, P. F., van den Oord, G., Dobber, M. R., Malkki, A., Visser, H., Vries, J. d., Stammes, P., Lundell, J., and Saari, H.: The ozone monitoring instrument, *IEEE Transactions on Geoscience and Remote Sensing*, 44, 1093–1101, <https://doi.org/10.1109/TGRS.2006.872333>, 2006.
- 680 Levelt, P. F., Joiner, J., Tamminen, J., Veefkind, J. P., Bhartia, P. K., Stein Zweers, D. C., Duncan, B. N., Streets, D. G., Eskes, H., van der A, R., McLinden, C., Fioletov, V., Carn, S., de Laat, J., DeLand, M., Marchenko, S., McPeters, R., Ziemke, J., Fu, D., Liu, X., Pickering, K., Apituley, A., González Abad, G., Arola, A., Boersma, F., Chan Miller, C., Chance, K., de Graaf, M., Hakkarainen, J., Hassinen, S., Ialongo, I., Kleipool, Q., Krotkov, N., Li, C., Lamsal, L., Newman, P., Nowlan, C., Suleiman, R., Tilstra, L. G., Torres, O., Wang, H., and Wargan, K.: The Ozone Monitoring Instrument: overview of 14 years in space, *Atmospheric Chemistry and Physics*, 18, 5699–5745, <https://doi.org/10.5194/acp-18-5699-2018>, 2018.
- 685

- Li, Y., Pickering, K. E., Allen, D. J., Barth, M. C., Bela, M. M., Cummings, K. A., Carey, L. D., Mecikalski, R. M., Fierro, A. O., Campos, T. L., Weinheimer, A. J., Diskin, G. S., and Biggerstaff, M. I.: Evaluation of deep convective transport in storms from different convective regimes during the DC3 field campaign using WRF-Chem with lightning data assimilation, *Journal of Geophysical Research: Atmospheres*, 122, 7140–7163, <https://doi.org/10.1002/2017JD026461>, 2017.
- 690 Li, Y., Pickering, K. E., Barth, M. C., Bela, M. M., Cummings, K. A., and Allen, D. J.: Evaluation of Parameterized Convective Transport of Trace Gases in Simulation of Storms Observed During the DC3 Field Campaign, *Journal of Geophysical Research: Atmospheres*, 123, 11,238–11,261, <https://doi.org/10.1029/2018JD028779>, 2018.
- Luo, C., Wang, Y., and Koshak, W. J.: Development of a self-consistent lightning NO<sub>x</sub> simulation in large-scale 3-D models, *Journal of Geophysical Research: Atmospheres*, 122, 3141–3154, <https://doi.org/10.1002/2016JD026225>, 2017.
- 695 Marais, E. A., Jacob, D. J., Choi, S., Joiner, J., Belmonte-Rivas, M., Cohen, R. C., Beirle, S., Murray, L. T., Schiferl, L., Shah, V., and Jaeglé, L.: Nitrogen oxides in the global upper troposphere: interpreting cloud-sliced NO<sub>2</sub> observations from the OMI satellite instrument, *Atmospheric Chemistry and Physics Discussions*, pp. 1–14, <https://doi.org/10.5194/acp-2018-556>, 2018.
- Martin, R. V., Sauvage, B., Folkens, I., Sioris, C. E., Boone, C., Bernath, P., and Ziemke, J.: Space-based constraints on the production of nitric oxide by lightning, *Journal of Geophysical Research*, 112, 1479, <https://doi.org/10.1029/2006JD007831>, 2007.
- 700 McKinney, W.: pandas: a foundational Python library for data analysis and statistics, *Python for High Performance and Scientific Computing*, 14, 2011.
- Mecikalski, R. M. and Carey, L. D.: Lightning characteristics relative to radar, altitude and temperature for a multicell, MCS and supercell over northern Alabama, *Atmospheric Research*, 191, 128–140, <https://doi.org/10.1016/j.atmosres.2017.03.001>, <http://www.sciencedirect.com/science/article/pii/S0169809516302812>, 2017.
- 705 Met Office: Cartopy: a cartographic python library with a matplotlib interface, Exeter, Devon, <http://scitools.org.uk/cartopy>, 2010 - 2015.
- Min, M., Wu, C., Li, C., Liu, H., Xu, N., Wu, X., Chen, L., Wang, F., Sun, F., Qin, D., Wang, X., Li, B., Zheng, Z., Cao, G., and Dong, L.: Developing the science product algorithm testbed for Chinese next-generation geostationary meteorological satellites: Fengyun-4 series, *JOURNAL OF METEOROLOGICAL RESEARCH*, 31, 708–719, <https://doi.org/10.1007/s13351-017-6161-z>, 2017.
- Myhre, G., Shindell, D., Bréon, F. M., Collins, W., Fuglestedt, J., Huang, J., Koch, D., Lamarque, J. F., Lee, D., and Mendoza, B.: Climate change 2013: the physical science basis. Contribution of Working Group I to the Fifth Assessment Report of the Intergovernmental Panel on Climate Change, K., Tignor, M., Allen, SK, Boschung, J., Nauels, A., Xia, Y., Bex, V., and Midgley, PM, Cambridge University Press Cambridge, United Kingdom and New York, NY, USA, 2013.
- 710 Nault, B. A., Garland, C., Wooldridge, P. J., Brune, W. H., Campuzano-Jost, P., Crounse, J. D., Day, D. A., Dibb, J., Hall, S. R., Huey, L. G., Jimenez, J. L., Liu, X., Mao, J., Mikoviny, T., Peischl, J., Pollack, I. B., Ren, X., Ryerson, T. B., Scheuer, E., Ullmann, K., Wennberg, P. O., Wisthaler, A., Zhang, L., and Cohen, R. C.: Observational Constraints on the Oxidation of NO<sub>x</sub> in the Upper Troposphere, *The Journal of Physical Chemistry A*, 120, 1468–1478, <https://doi.org/10.1021/acs.jpca.5b07824>, 2016.
- 715 Nault, B. A., Laughner, J. L., Wooldridge, P. J., Crounse, J. D., Dibb, J., Diskin, G., Peischl, J., Podolske, J. R., Pollack, I. B., Ryerson, T. B., Scheuer, E., Wennberg, P. O., and Cohen, R. C.: Lightning NO<sub>x</sub> Emissions: Reconciling Measured and Modeled Estimates With Updated NO<sub>x</sub> Chemistry, *Geophysical Research Letters*, 44, 9479–9488, <https://doi.org/10.1002/2017GL074436>, 2017.
- 720 Ott, L. E., Pickering, K. E., Stenichkov, G. L., Huntrieser, H., and Schumann, U.: Effects of lightning NO<sub>x</sub> production during the 21 July European Lightning Nitrogen Oxides Project storm studied with a three-dimensional cloud-scale chemical transport model, *Journal of Geophysical Research*, 112, 61, <https://doi.org/10.1029/2006JD007365>, 2007.

- Ott, L. E., Pickering, K. E., Stenchikov, G. L., Allen, D. J., DeCaria, A. J., Ridley, B., Lin, R.-F., Lang, S., and Tao, W.-K.: Production of lightning  $\text{NO}_x$  and its vertical distribution calculated from three-dimensional cloud-scale chemical transport model simulations, *Journal of Geophysical Research*, 115, 4711, <https://doi.org/10.1029/2009JD011880>, 2010.
- Pickering, K. E., Thompson, A. M., Wang, Y., Tao, W.-K., McNamara, D. P., Kirchoff, V. W. J. H., Heikes, B. G., Sachse, G. W., Bradshaw, J. D., Gregory, G. L., and Blake, D. R.: Convective transport of biomass burning emissions over Brazil during TRACE A, *Journal of Geophysical Research*, 101, 23 993–24 012, <https://doi.org/10.1029/96JD00346>, 1996.
- Pickering, K. E., Bucsele, E., Allen, D., Ring, A., Holzworth, R., and Krotkov, N.: Estimates of lightning  $\text{NO}_x$  production based on OMI  $\text{NO}_2$  observations over the Gulf of Mexico, *Journal of Geophysical Research: Atmospheres*, 121, 8668–8691, <https://doi.org/10.1002/2015JD024179>, 2016.
- Platt, U. and Perner, D.: Measurements of Atmospheric Trace Gases by Long Path Differential UV/Visible Absorption Spectroscopy, in: *Optical and Laser Remote Sensing*, edited by Schawlow, A. L., Killinger, D. K., and Mooradian, A., vol. 39 of *Springer Series in Optical Sciences*, pp. 97–105, Springer Berlin Heidelberg, Berlin, Heidelberg, [https://doi.org/10.1007/978-3-540-39552-2\\_13](https://doi.org/10.1007/978-3-540-39552-2_13), 1983.
- Price, C. and Rind, D.: A simple lightning parameterization for calculating global lightning distributions, *Journal of Geophysical Research*, 97, 9919–9933, <https://doi.org/10.1029/92JD00719>, 1992.
- Richter, A., Burrows, J. P., Nüß, H., Granier, C., and Niemeier, U.: Increase in tropospheric nitrogen dioxide over China observed from space, *Nature*, 437, 129–132, <https://doi.org/10.1038/nature04092>, 2005.
- Romps, D. M.: Evaluating the future of lightning in cloud-resolving models, *Geophysical Research Letters*, <https://doi.org/10.1029/2019GL085748>, 2019.
- Romps, D. M., Seeley, J. T., Vollaro, and Molinari, J.: Projected increase in lightning strikes in the United States due to global warming, *Atmospheric Chemistry and Physics*, 346, 851–854, <https://doi.org/10.1126/science.1259100>, 2014.
- Rudlosky, S.: Evaluating ENTLN performance relative to TRMM/LIS, *Journal of Operational Meteorology*, 3, 11–20, <https://doi.org/10.15191/nwajom.2015.0302>, 2015.
- Schaaf, C. B., Liu, J., Gao, F., and Strahler, A. H.: Aqua and Terra MODIS Albedo and Reflectance Anisotropy Products, in: *Land Remote Sensing and Global Environmental Change*, edited by Ramachandran, B., Justice, C. O., and Abrams, M. J., vol. 11 of *Remote Sensing and Digital Image Processing*, pp. 549–561, Springer New York, New York, NY, [https://doi.org/10.1007/978-1-4419-6749-7\\_24](https://doi.org/10.1007/978-1-4419-6749-7_24), 2011.
- Schumann, U. and Huntrieser, H.: The global lightning-induced nitrogen oxides source, *Atmospheric Chemistry and Physics*, 7, 3823–3907, <https://doi.org/10.5194/acp-7-3823-2007>, 2007.
- Schwantes, R. H., Teng, A. P., Nguyen, T. B., Coggon, M. M., Crouse, J. D., St Clair, J. M., Zhang, X., Schilling, K. A., Seinfeld, J. H., and Wennberg, P. O.: Isoprene  $\text{NO}_3$  Oxidation Products from the  $\text{RO}_2 + \text{HO}_2$  Pathway, *The Journal of Physical Chemistry A*, 119, 10 158–10 171, <https://doi.org/10.1021/acs.jpca.5b06355>, 2015.
- Seabold, S. and Perktold, J.: statsmodels: Econometric and statistical modeling with python, in: 9th Python in Science Conference, 2010.
- Silvern, R. F., Jacob, D. J., Travis, K. R., Sherwen, T., Evans, M. J., Cohen, R. C., Laughner, J. L., Hall, S. R., Ullmann, K., Crouse, J. D., Wennberg, P. O., Peischl, J., and Pollack, I. B.: Observed  $\text{NO}/\text{NO}_2$  ratios in the upper troposphere imply errors in  $\text{NO}-\text{NO}_2-\text{O}_3$  cycling kinetics or an unaccounted  $\text{NO}_x$  reservoir, *Geophysical Research Letters*, <https://doi.org/10.1029/2018GL077728>, 2018.
- Sneep, M., de Haan, J. F., Stammes, P., Wang, P., Vanbauce, C., Joiner, J., Vasilkov, A. P., and Levelt, P. F.: Three-way comparison between OMI and PARASOL cloud pressure products, *Journal of Geophysical Research*, 113, D05 204, <https://doi.org/10.1029/2007JD008694>, 2008.



- 760 Stammes, P., Sneep, M., de Haan, J. F., Veefkind, J. P., Wang, P., and Levelt, P. F.: Effective cloud fractions from the Ozone Monitoring Instrument: Theoretical framework and validation, *Journal of Geophysical Research*, 113, D05 204, <https://doi.org/10.1029/2007JD008820>, 2008.
- Strode, S. A., Douglass, A. R., Ziemke, J. R., Manyin, M., Nielsen, J. E., and Oman, L. D.: A Model and Satellite-Based Analysis of the Tropospheric Ozone Distribution in Clear Versus Convectively Cloudy Conditions, *Journal of Geophysical Research: Atmospheres*, 122, 11,948–11,960, <https://doi.org/10.1002/2017JD027015>, 2017.
- 765 Travis, K. R., Jacob, D. J., Fisher, J. A., Kim, P. S., Marais, E. A., Zhu, L., Yu, K., Miller, C. C., Yantosca, R. M., Sulprizio, M. P., Thompson, A. M., Wennberg, P. O., Crounse, J. D., St Clair, J. M., Cohen, R. C., Laughner, J. L., Dibb, J. E., Hall, S. R., Ullmann, K., Wolfe, G. M., Pollack, I. B., Peischl, J., Neuman, J. A., and Zhou, X.: Why do Models Overestimate Surface Ozone in the Southeastern United States?, *Atmospheric Chemistry and Physics*, 16, 13 561–13 577, <https://doi.org/10.5194/acp-16-13561-2016>, 2016.
- 770 van der Walt, S., Colbert, S. C., and Varoquaux, G.: The NumPy Array: A Structure for Efficient Numerical Computation, *Computing in Science & Engineering*, 13, 22–30, <https://doi.org/10.1109/MCSE.2011.37>, 2011.
- Vasilkov, A., Joiner, J., Spurr, R., Bhartia, P. K., Levelt, P., and Stephens, G.: Evaluation of the OMI cloud pressures derived from rotational Raman scattering by comparisons with other satellite data and radiative transfer simulations, *Journal of Geophysical Research*, 113, D05 204, <https://doi.org/10.1029/2007JD008689>, 2008.
- 775 Veefkind, J. P., Aben, I., McMullan, K., Förster, H., de Vries, J., Otter, G., Claas, J., Eskes, H. J., de Haan, J. F., Kleipool, Q., van Weele, M., Hasekamp, O., Hoogeveen, R., Landgraf, J., Snel, R., Tol, P., Ingmann, P., Voors, R., Kruizinga, B., Vink, R., Visser, H., and Levelt, P. F.: TROPOMI on the ESA Sentinel-5 Precursor: A GMES mission for global observations of the atmospheric composition for climate, air quality and ozone layer applications, *Remote Sensing of Environment*, 120, 70–83, <https://doi.org/10.1016/j.rse.2011.09.027>, 2012.
- Wang, L., Follette-Cook, M. B., Newchurch, M. J., Pickering, K. E., Pour-Biazar, A., Kuang, S., Koshak, W., and Peterson, H.: Evaluation of lightning-induced tropospheric ozone enhancements observed by ozone lidar and simulated by WRF/Chem, *Atmospheric Environment*, 115, 185–191, <https://doi.org/10.1016/j.atmosenv.2015.05.054>, 2015.
- 780 Waskom, M., Botvinnik, O., O’Kane, D., Hobson, P., Lukauskas, S., Gemperline, D. C., Augspurger, T., Halchenko, Y., Cole, J. B., Warmenhoven, J., de Ruiter, J., Pye, C., Hoyer, S., Vanderplas, J., Villalba, S., Kunter, G., Quintero, E., Bachant, P., Martin, M., Meyer, K., Miles, A., Ram, Y., Yarkoni, T., Williams, M. L., Evans, C., Fitzgerald, C., Brian, F., Fonesbeck, C., Lee, A., and Qalieh, A.: Mwaskom/Seaborn: V0.8.1 (September 2017), <https://doi.org/10.5281/zenodo.883859>, 2017.
- 785 Williams, E. R.: The tripole structure of thunderstorms, *Journal of Geophysical Research*, 94, 13 151, <https://doi.org/10.1029/JD094iD11p13151>, 1989.
- Wong, J., Barth, M. C., and Noone, D.: Evaluating a lightning parameterization based on cloud-top height for mesoscale numerical model simulations, *Geoscientific Model Development*, 6, 429–443, <https://doi.org/10.5194/gmd-6-429-2013>, 2013.
- 790 Xu, K.-M. and Randall, D. A.: A Semiempirical Cloudiness Parameterization for Use in Climate Models, *Journal of the Atmospheric Sciences*, 53, 3084–3102, [https://doi.org/10.1175/1520-0469\(1996\)053<3084:ASCPFU>2.0.CO;2](https://doi.org/10.1175/1520-0469(1996)053<3084:ASCPFU>2.0.CO;2), 1996.
- Yang, J., Zhang, Z., Wei, C., Lu, F., and Guo, Q.: Introducing the New Generation of Chinese Geostationary Weather Satellites, Fengyun-4, *Bulletin of the American Meteorological Society*, 98, 1637–1658, <https://doi.org/10.1175/BAMS-D-16-0065.1>, 2017.
- 795 Zel’dovich, Y. and Raizer, Y.: VIII - Physical and chemical kinetics in hydrodynamic processes, in: *Physics of Shock Waves and High-Temperature Hydrodynamic Phenomena*, edited by Hayes, W. D., Probstein, R. F., Zel’dovich, Y., and Raizer, Y., pp. 566–571, Academic Press, <https://doi.org/10.1016/B978-0-12-395672-9.50009-6>, 1967.

- Zhang, P., Lu, Q., Hu, X., Gu, S., Yang, L., Min, M., Chen, L., Xu, N., Sun, L., Bai, W., Ma, G., and Di Xian: Latest Progress of the Chinese Meteorological Satellite Program and Core Data Processing Technologies, *Advances in Atmospheric Sciences*, 36, 1027–1045, <https://doi.org/10.1007/s00376-019-8215-x>, 2019.
- 800 Zhang, X. and Laughner, J.: zxdawn/BEHR-LNOx: v1.0, Zenodo, <https://doi.org/10.5281/zenodo.3553426>, 2019.
- Zhao, C., Wang, Y., Choi, Y., and Zeng, T.: Summertime impact of convective transport and lightning NO<sub>x</sub> production over North America: modeling dependence on meteorological simulations, *Atmospheric Chemistry and Physics*, 9, 4315–4327, <https://doi.org/10.5194/acp-9-4315-2009>, 2009.
- Zhou, Y., Brunner, D., Boersma, K. F., Dirksen, R., and Wang, P.: An improved tropospheric NO<sub>2</sub> retrieval for OMI observations in the vicinity of mountainous terrain, *Atmospheric Measurement Techniques*, 2, 401–416, <https://doi.org/10.5194/amt-2-401-2009>, 2009.
- 805 Zhu, Q., Laughner, J. L., and Cohen, R. C.: Lightning NO<sub>2</sub> simulation over the contiguous US and its effects on satellite NO<sub>2</sub> retrievals, *Atmospheric Chemistry and Physics*, 19, 13 067–13 078, <https://doi.org/10.5194/acp-19-13067-2019>, 2019.
- Zhu, Y., Rakov, V. A., Tran, M. D., and Nag, A.: A study of National Lightning Detection Network responses to natural lightning based on ground truth data acquired at LOG with emphasis on cloud discharge activity, *Journal of Geophysical Research: Atmospheres*, 121, 14,651–14,660, <https://doi.org/10.1002/2016JD025574>, 2016.
- 810 Zhu, Y., Rakov, V. A., Tran, M. D., Stock, M. G., Heckman, S., Liu, C., Sloop, C. D., Jordan, D. M., Uman, M. A., Caicedo, J. A., Kotovsky, D. A., Wilkes, R. A., Carvalho, F. L., Ngin, T., Gamerota, W. R., Pilkey, J. T., and Hare, B. M.: Evaluation of ENTLN Performance Characteristics Based on the Ground Truth Natural and Rocket-Triggered Lightning Data Acquired in Florida, *Journal of Geophysical Research: Atmospheres*, 122, 9858–9866, <https://doi.org/10.1002/2017JD027270>, 2017.
- 815 Ziemke, J. R., Joiner, J., Chandra, S., Bhartia, P. K., Vasilkov, A., Haffner, D. P., Yang, K., Schoeberl, M. R., Froidevaux, L., and Levelt, P. F.: Ozone mixing ratios inside tropical deep convective clouds from OMI satellite measurements, *Atmospheric Chemistry and Physics*, 9, 573–583, <https://doi.org/10.5194/acp-9-573-2009>, 2009.
- Ziemke, J. R., Strode, S. A., Douglass, A. R., Joiner, J., Vasilkov, A., Oman, L. D., Liu, J., Strahan, S. E., Bhartia, P. K., and Haffner, D. P.: A cloud-ozone data product from Aura OMI and MLS satellite measurements, *Atmospheric Measurement Techniques*, 10, 4067–4078, <https://doi.org/10.5194/amt-10-4067-2017>, 2017.
- 820

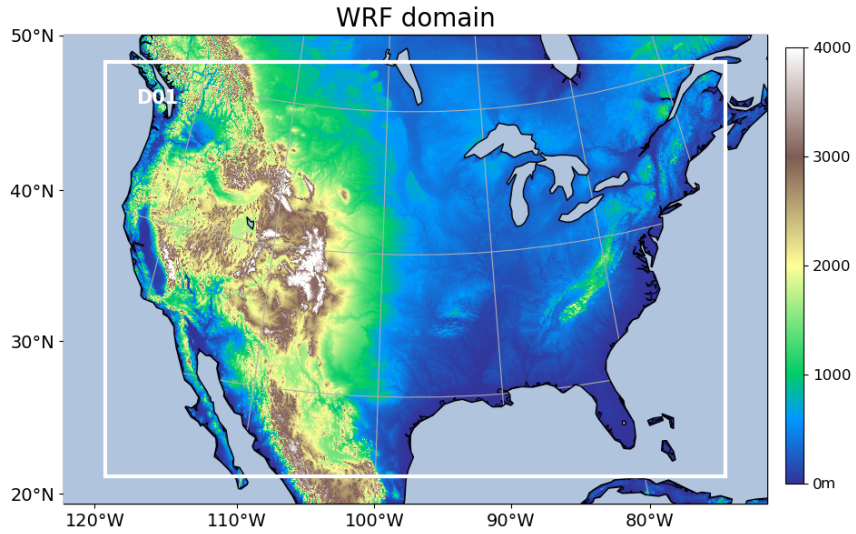


**Figure 1.** Domain and terrain height (m) of the WRF-Chem simulation with 350 x 290 grid cells and a horizontal resolution of 12 km.

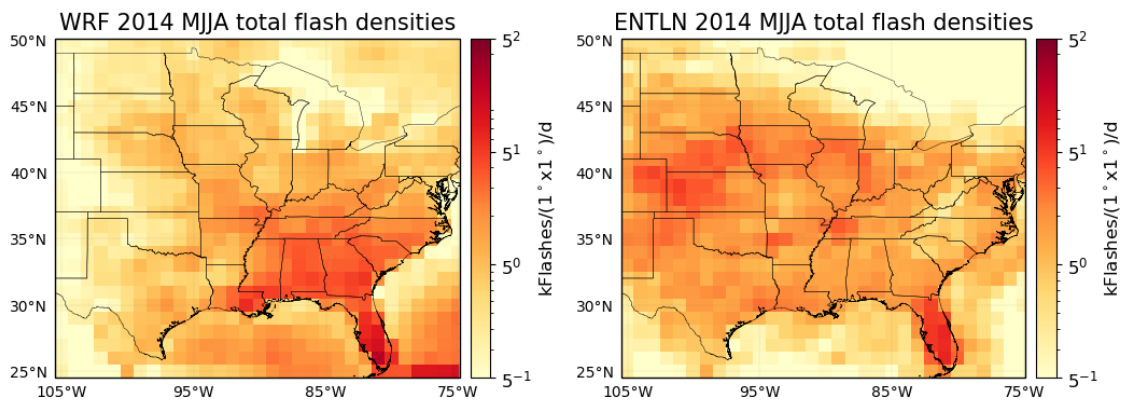


**Figure 2.** Comparison between total flash densities from ENTLN and WRF-Chem during MJJA 2014.

**Table 1.** Definitions of the abbreviations for the criteria used in this study.

Abbreviations	Full form [source]
CRF	Cloud radiance fraction [OMI]
CP	Cloud optical pressure [OMI]
CF	Cloud fraction [WRF-Chem]
TL	Total lightning flashes [WRF-Chem]
ratio	modeled LNO <sub>2</sub> Vis / modeled NO <sub>2</sub> Vis [WRF-Chem]
CRF <sub>α</sub> _ENTLN	CRF ≥ α + ENTLN flashes(strokes) ≥ 2400(8160) [ENTLN]
CRF <sub>α</sub> _CF40_ENTLN	CRF ≥ α + ENTLN flashes(strokes) ≥ 2400(8160) + CF ≥ 40%
CRF <sub>α</sub> _ENTLN_TL1000	CRF ≥ α + ENTLN flashes(strokes) ≥ 2400(8160) + TL ≥ 1000
CRF <sub>α</sub> _CF40_ENTLN_TL1000	CRF ≥ α + ENTLN flashes(strokes) ≥ 2400(8160) + CF ≥ 40% + TL ≥ 1000
CRF <sub>α</sub> _ENTLN_TL1000_ratio50	CRF ≥ α + ENTLN flashes(strokes) ≥ 2400(8160) + TL ≥ 1000 + ratio ≥ 50%
CRF <sub>α</sub> _CF40_ENTLN_TL1000_ratio50	CRF ≥ α + ENTLN flashes(strokes) ≥ 2400(8160) + CF ≥ 40% + TL ≥ 1000 + ratio ≥ 50%
CRF <sub>α</sub> _ENTLN1(3.4)_TL1_ratio50	CRF ≥ α + ENTLN flashes(strokes) ≥ 1(3.4) + TL ≥ 1 + ratio ≥ 50%

α has three options: 70%, 90% and 100%

**Table 2.** LNO<sub>x</sub> production efficiencies for different combinations of criteria defined in Table 1.

Condition <sup>1</sup>	ENTLN data type <sup>2</sup>	LNO <sub>x</sub> /flash or LNO <sub>x</sub> /stroke	R value	Intercept (10 <sup>6</sup> mol)	Days <sup>3</sup>
CRF90_ENTLN	Flash	52.1 ± 51.1	0.20	0.21	99
CRF90_CF40_ENTLN	Flash	84.2 ± 31.5	0.54	-0.04	70
CRF90_ENTLN_TL1000	Flash	61.9 ± 49.1	0.27	0.33	83
CRF90_CF40_ENTLN_TL1000	Flash	63.4 ± 52.9	0.38	0.26	38
CRF90_ENTLN_TL1000_ratio50	Flash	54.5 ± 48.1	0.25	0.39	81
CRF90_CF40_ENTLN_TL1000_ratio50	Flash	90.0 ± 65.0	0.46	0.15	32
CRF90_ENTLN	Stroke	6.7 ± 4.1	0.31	0.23	102
CRF90_CF40_ENTLN	Stroke	10.3 ± 3.6	0.55	0.08	79
CRF90_ENTLN_TL1000	Stroke	7.5 ± 5.1	0.29	0.38	94
CRF90_CF40_ENTLN_TL1000	Stroke	8.6 ± 6.2	0.39	0.27	46
CRF90_ENTLN_TL1000_ratio50	Stroke	7.0 ± 4.8	0.29	0.42	93
CRF90_CF40_ENTLN_TL1000_ratio50	Stroke	8.9 ± 7.0	0.39	0.31	40

<sup>1</sup>These conditions are defined in Table 1. <sup>2</sup>The thresholds of ENTLN data are 2400 flashes box<sup>-1</sup> and 8160 strokes box<sup>-1</sup> during the period of 2.4 h before OMI overpass time. <sup>3</sup>The number of valid days with specific criteria in MJJA 2014.

**Table 3.** LNO<sub>x</sub> production efficiencies for different thresholds of CRF with coincident ENTLN data, TL ≥ 1000 and ratio ≥ 50%.

CRF (%)	ENTLN data type <sup>1</sup>	LNO <sub>x</sub> /flash or LNO <sub>x</sub> /stroke	R value	Intercept (10 <sup>5</sup> mol)	Days <sup>2</sup>
70	Flash	35.7 ± 36.8	0.21	4.91	85
90	Flash	54.5 ± 48.1	0.25	3.90	81
100	Flash	20.8 ± 37.4	0.13	5.67	71
70	Stroke	4.1 ± 3.9	0.21	5.16	96
90	Stroke	7.0 ± 4.8	0.29	4.16	93
100	Stroke	2.6 ± 4.0	0.14	5.41	82

<sup>1</sup>The thresholds of ENTLN data are 2400 flashes box<sup>-1</sup> and 8160 strokes box<sup>-1</sup> during the period of 2.4 h before OMI overpass time. <sup>2</sup>The number of valid days with specific criteria in MJJA 2014.

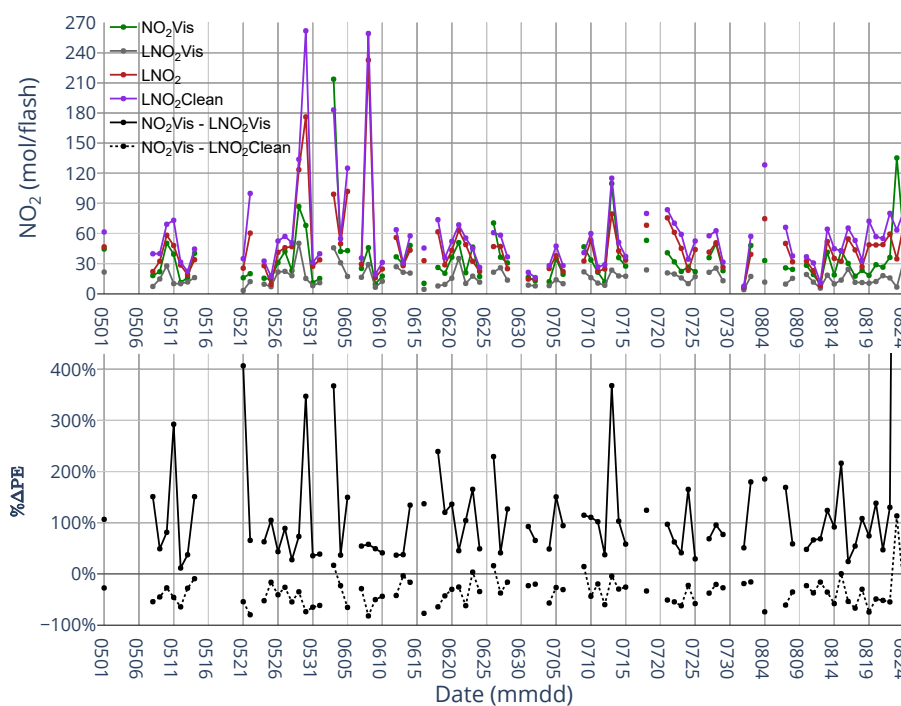


**Figure 3.** (top) Time series of NO<sub>2</sub>Vis, LNO<sub>2</sub>Vis, LNO<sub>2</sub> and LNO<sub>2</sub>Clean production per day over the CONUS for MJJA 2014 with CRF ≥ 90% and a flash threshold of 2400 flashes per 2.4 h. (bottom) Time series of the percent differences between NO<sub>2</sub>Vis and LNO<sub>2</sub>Vis and the percent differences between NO<sub>2</sub>Vis and LNO<sub>2</sub>Clean with CRF ≥ 90%. The value of black dot on August 23 (not shown) is 1958%.

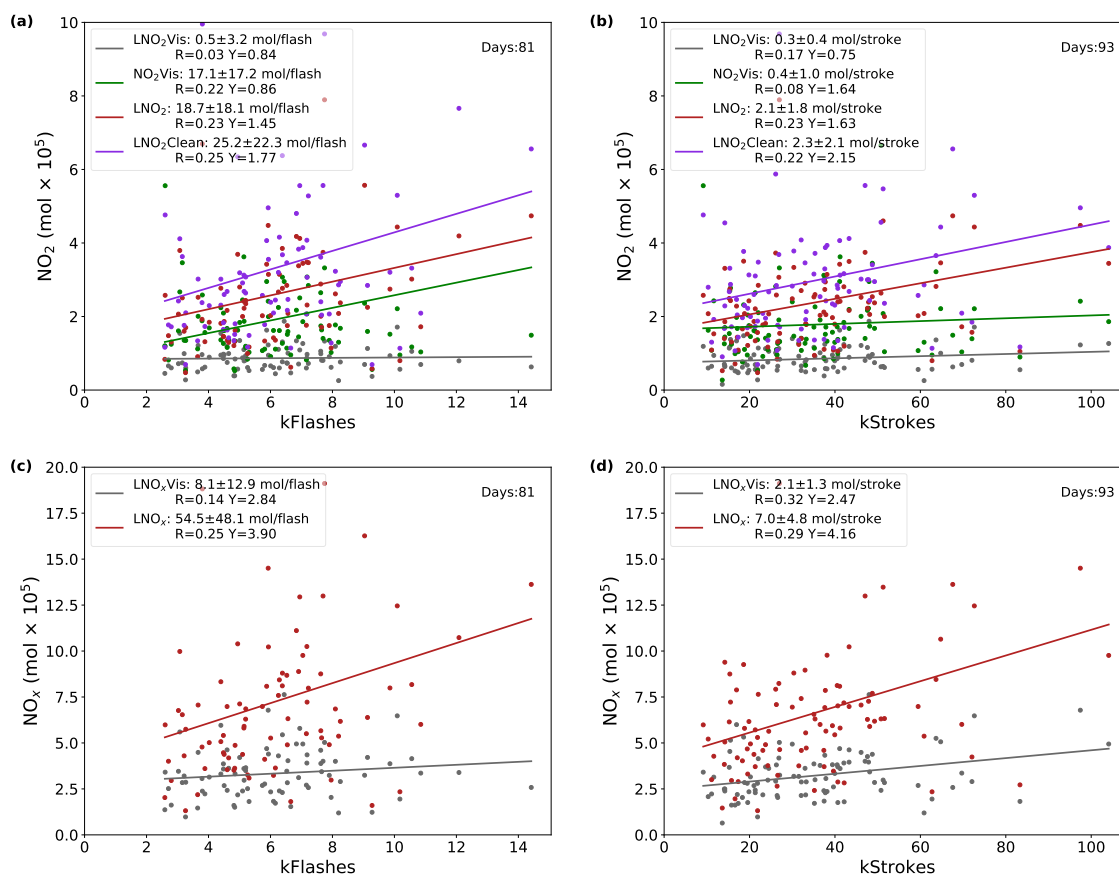


**Figure 4.** (a) Daily  $\text{NO}_2\text{Vis}$ ,  $\text{LNO}_2\text{Vis}$ ,  $\text{LNO}_2$  and  $\text{LNO}_2\text{Clean}$  versus ENTLN total flashes data. (b) Same as (a) but for strokes. (c) Daily  $\text{LNO}_x\text{Vis}$  and  $\text{LNO}_x$  versus total flashes. (d) Same as (c) but for strokes.

**Table 4.** The percent changes in the estimated production when using different methods based on the same a priori profiles.

	City <sup>1</sup>	$(\text{LNO}_2\text{Clean} - \text{LNO}_2)/\text{LNO}_2$	$(\text{LNO}_2 - \text{TropVis})/\text{TropVis}$	$(\text{LNO}_2\text{Clean} - \text{TropVis})/\text{TropVis}$
<b>Polluted</b>	Lansing	24.2%	49.5%	85.6%
	New Orleans	13.3%	121.2%	153.8%
	Orlando	46.3%	37.5%	101.3%
<b>Clean</b>	Huron	12.0%	56.4%	75.2%
	Charles Town	12.0%	82.2%	104.1%
	Tarboro	5.0%	86.0%	95.3%

<sup>1</sup> Locations are denoted in Fig. 6a.

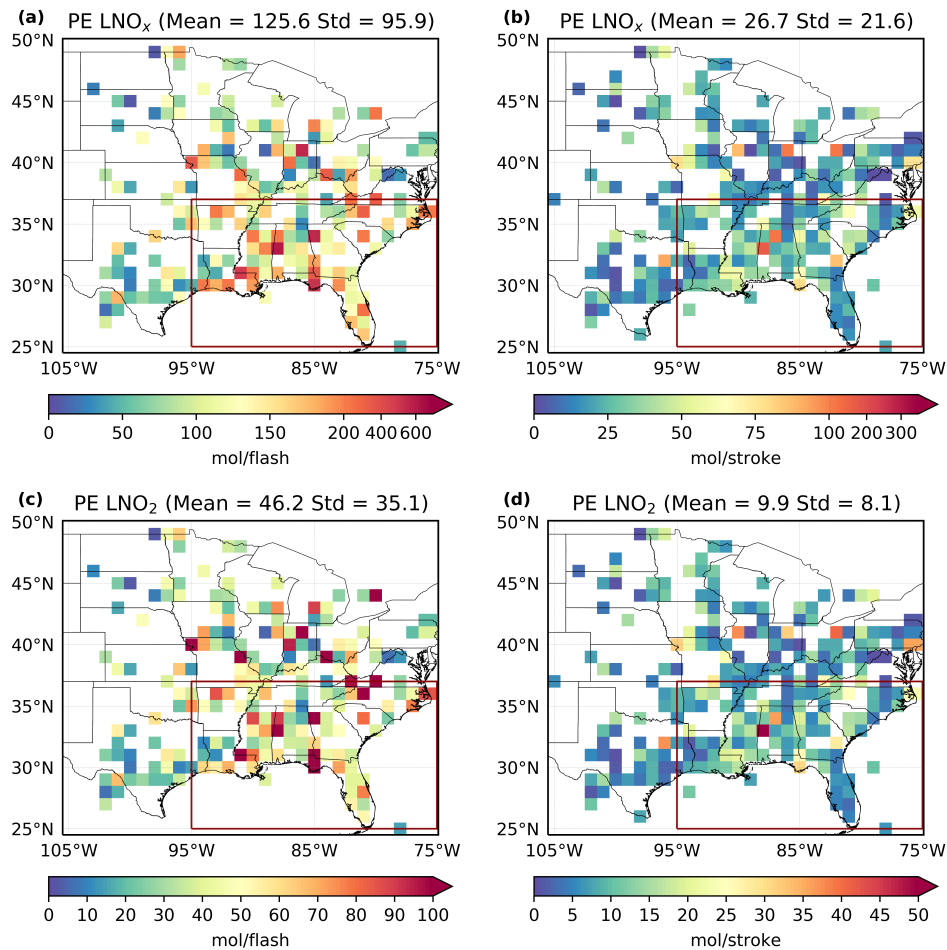


**Figure 5.** (a) and (c) Maps of  $1^\circ \times 1^\circ$  gridded values of mean LNO<sub>x</sub> and LNO<sub>2</sub> production per flash with CRF  $\geq 90\%$  for MJJA 2014. (b) and (d) Same as (a) and (c) except for strokes. The southeastern US is denoted by the red box in panels a – d.

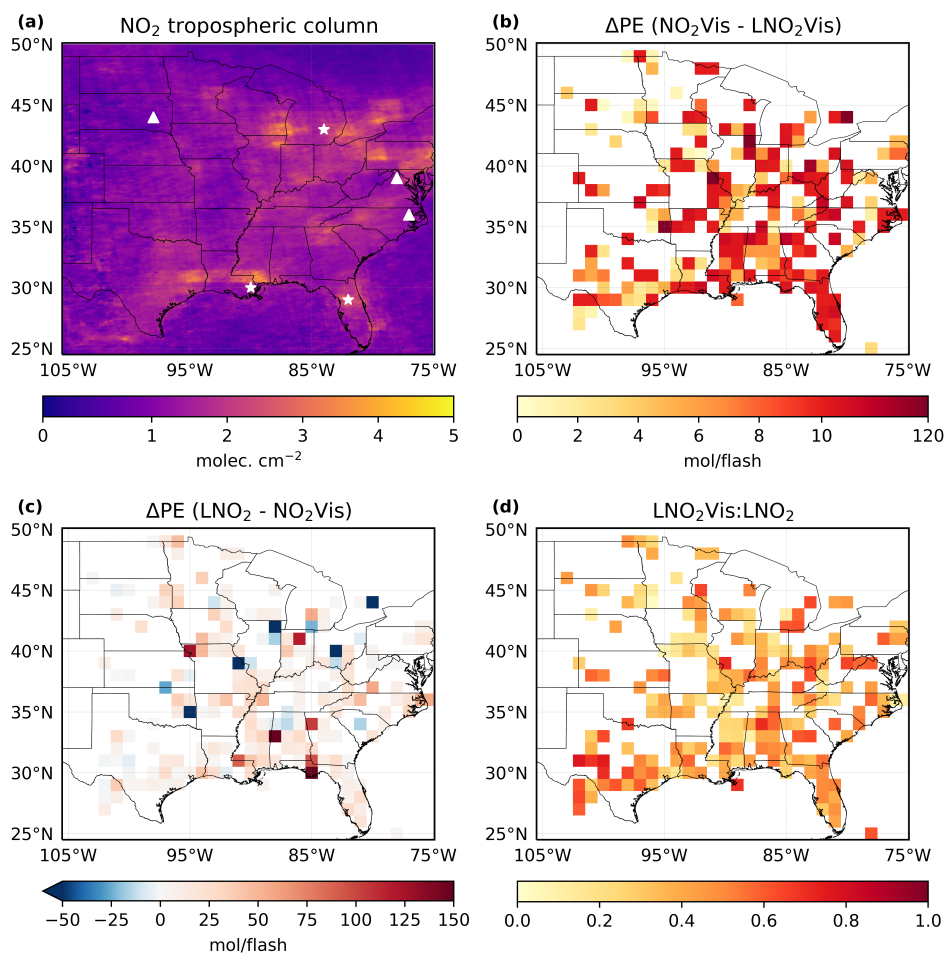


**Figure 6.** (a) Mean (MJJA 2014) NO<sub>2</sub> tropospheric column. Polluted cities are denoted by stars: Lansing, New Orleans and Orlando while clean cities are denoted by triangles: Huron, Charles Town and Tarboro. (b) The differences of the estimated mean production efficiency between NO<sub>2</sub>Vis and LNO<sub>2</sub>Vis with CRF ≥ 90%. (c) The same differences as (b) but between LNO<sub>2</sub> and NO<sub>2</sub>Vis. (d) The ratio of LNO<sub>2</sub>Vis to LNO<sub>2</sub>.



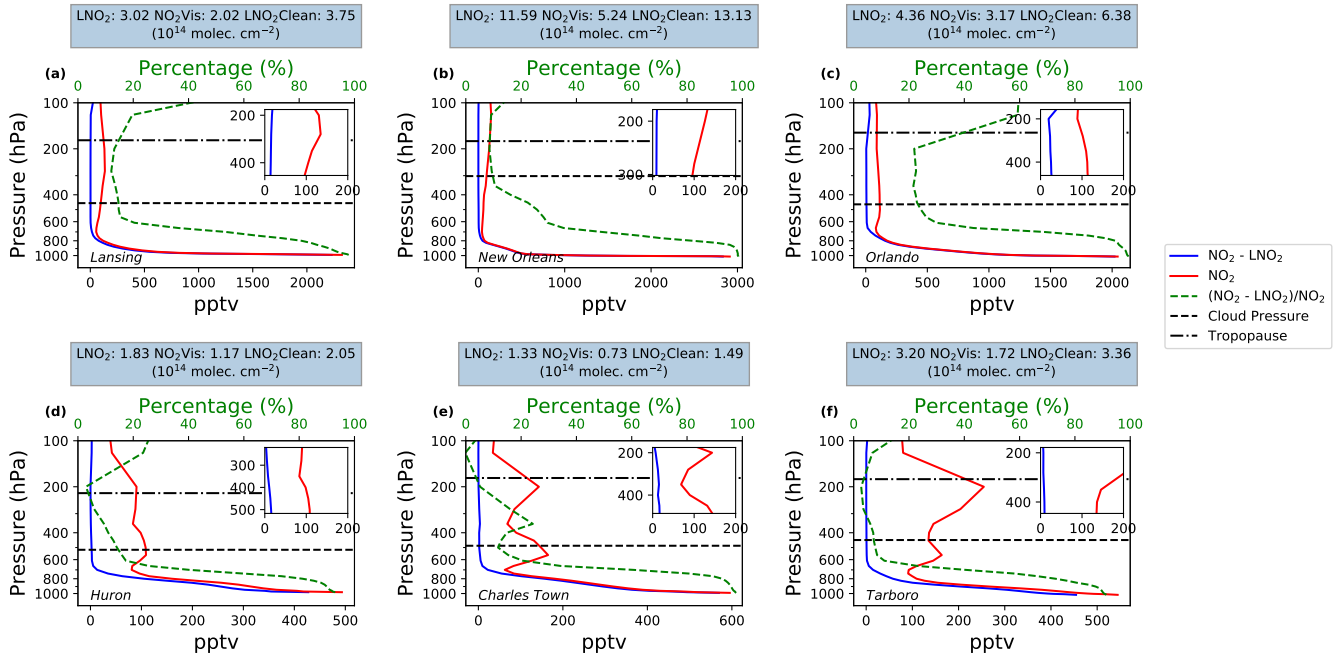


**Figure 7.** Comparisons of mean WRF-Chem  $\text{NO}_2$  and background  $\text{NO}_2$  profiles in six grids with  $\text{CRF} \geq 100\%$  on specific days during MJJA 2014. The top row data are selected from polluted regions (stars in Fig. 6a) while the bottom row data are from clean regions (triangles in Fig. 6a). The green dashed lines are the mean ratio profiles of background  $\text{NO}_2$  to total  $\text{NO}_2$ . The zoomed figures show the profiles from the cloud pressure to the tropopause. The titles present the mean productions based on three different methods mentioned in Sect. 2.4.

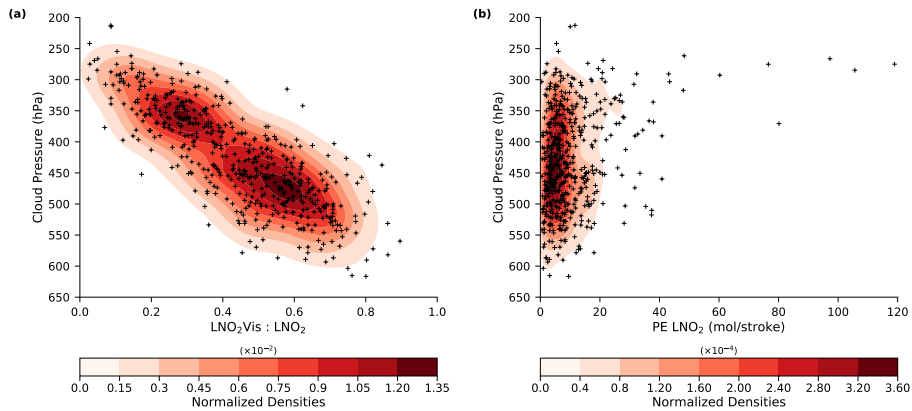


**Figure 8.** Kernel density estimation of the (a) daily ratio of  $\text{LNO}_2\text{Vis}$  to  $\text{LNO}_2$  and (b) daily  $\text{LNO}_2$  production efficiency versus the daily cloud pressure measured by OMI with  $\text{CRF} \geq 90\%$  for MJJA 2014. The kernel density estimation was generated by kdeplot in the Python package named seaborn.

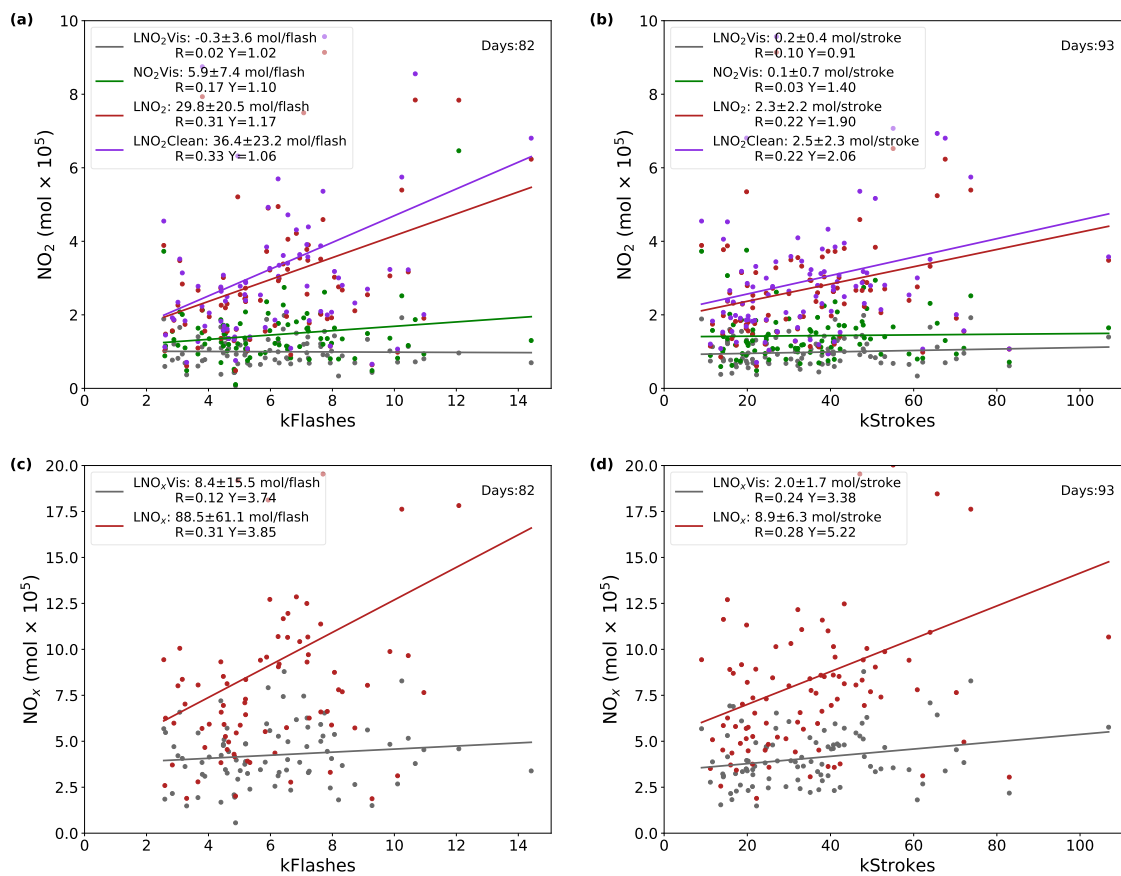


**Figure 9.** Same as Fig. 4 except for the  $2 \times 500$  mol NO flash<sup>-1</sup> configuration.

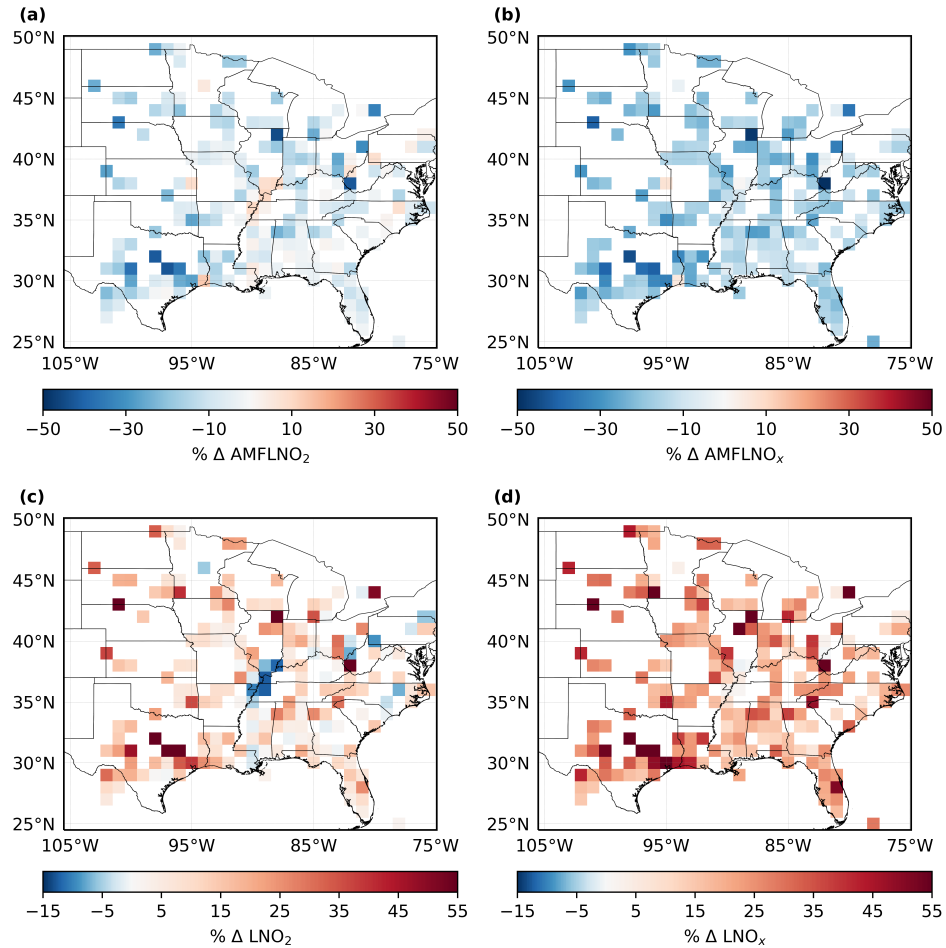


**Figure 10.** Average percent differences in (a)  $AMFLNO_2$ , (b)  $AMFLNO_x$ , (c)  $LNO_2$  and (d)  $LNO_x$  with  $CRF \geq 90\%$  over MJJA 2014. Differences between profiles are generated by  $2 \times 500 \text{ mol NO flash}^{-1}$  and  $1 \times 200 \text{ mol NO flash}^{-1}$ .

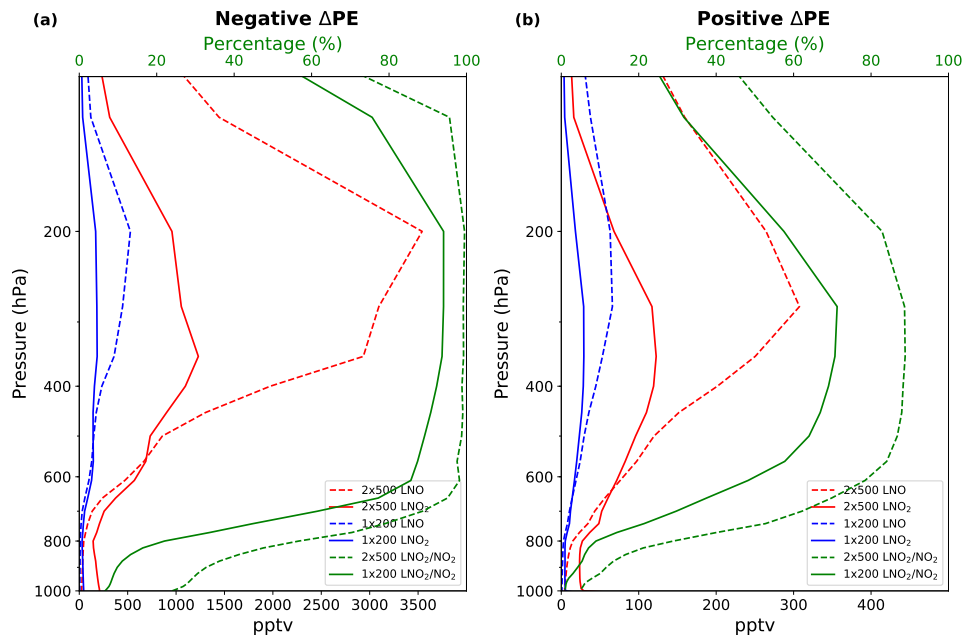


**Figure 11.** LNO and LNO<sub>2</sub> profiles with different LNO settings at (a) the region containing the minimal negative percent change in LNO<sub>2</sub> and (b) the region containing the largest positive percent change in LNO<sub>2</sub> when the LNO setting is changed from 1×200 mol NO flash<sup>-1</sup> to 2×500 mol NO flash<sup>-1</sup>, averaged over MJJA 2014. The profiles using 1×200 (2×500) mol NO flash<sup>-1</sup> are shown in blue (red) lines. Solid (dashed) green lines are the mean ratio of LNO<sub>2</sub> to NO<sub>2</sub> with 1×200 (2×500) mol NO flash<sup>-1</sup>.

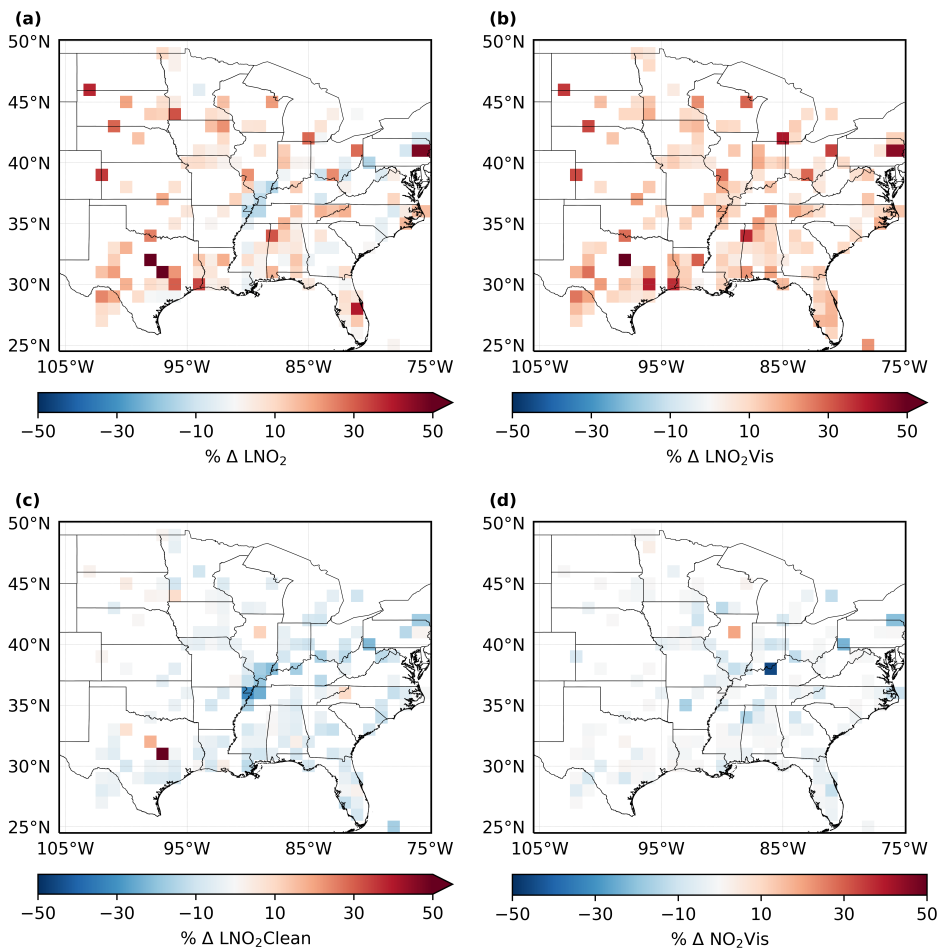


**Figure 12.** Average percent differences in (a) LNO<sub>2</sub>, (b) LNO<sub>2</sub> Vis, (c) LNO<sub>2</sub> Clean and (d) NO<sub>2</sub> Vis with CRF = 100% over MJJA 2014.

**Table 5.** Uncertainties for the estimation of LNO<sub>2</sub>/flash, LNO<sub>x</sub>/flash, LNO<sub>2</sub>/stroke and LNO<sub>x</sub>/stroke.

Type	Perturbation	LNO <sub>2</sub> /flash <sup>5</sup>	LNO <sub>x</sub> /flash <sup>5</sup>	LNO <sub>2</sub> /stroke <sup>5</sup>	LNO <sub>x</sub> /stroke <sup>5</sup>
BEHR tropopause pressure <sup>1</sup>	NASA product tropopause	6	4	6	4
Cloud radiance fraction <sup>1</sup>	± 5%	2	2	2	2
Cloud pressure <sup>2</sup>	Variable	32	34	32	34
Surface pressure <sup>1</sup>	± 1.5%	0	0	0	0
Surface reflectivity <sup>1</sup>	± 17%	0	0	0	0
LNO <sub>2</sub> profile <sup>1</sup>	2×500 mol NO flash <sup>-1</sup>	13	25	13	25
Profile location <sup>1</sup>	Quasi-Monte Carlo	0	1	0	1
Lightning detection efficiency <sup>3</sup>	IC: ± 16%, CG: ± 5%	15	15	15	15
t <sub>window</sub> <sup>3</sup>	2 – 4 hours	10	10	8	8
LNO <sub>x</sub> lifetime <sup>3</sup>	2 – 12 hours	24	24	24	24
V <sub>strat</sub> <sup>4</sup>	-	10	10	10	10
Systematic errors in slant column <sup>4</sup>	-	5	5	5	5
Tropospheric background <sup>4</sup>	-	10	10	10	10
NO/NO <sub>2</sub> <sup>4</sup>	20% ± 15%	0	15	0	15
Net	-	49	56	48	56

PE<sub>uncertainty</sub> = (Error<sub>rising perturbed value</sub> - Error<sub>lowering perturbed value</sub>)/2 where Error<sub>perturbed value</sub> = (PE<sub>perturbed value</sub> - PE<sub>original value</sub>)/PE<sub>original value</sub>.

<sup>1</sup>Laughner et al. (2019) <sup>2</sup>Acarreta et al. (2004) <sup>3</sup>Lapierre et al. (2020) <sup>4</sup>Allen et al. (2019) and Bucsele et al. (2019) <sup>5</sup>Uncertainty (%)

**Table A1.** Simple forms of abbreviations for AMFs.

Abbreviations	Numerator <sup>1</sup>	Denominator <sup>2</sup>
AMF <sub>LNO<sub>2</sub></sub>	S <sub>NO<sub>2</sub></sub>	V <sub>LNO<sub>2</sub></sub>
AMF <sub>LNO<sub>2</sub>Vis</sub>	S <sub>NO<sub>2</sub></sub>	V <sub>LNO<sub>2</sub>Vis</sub>
AMF <sub>LNO<sub>2</sub>Clean</sub>	S <sub>LNO<sub>2</sub></sub>	V <sub>LNO<sub>2</sub></sub>
AMF <sub>NO<sub>2</sub>Vis</sub>	S <sub>NO<sub>2</sub></sub>	V <sub>NO<sub>2</sub>Vis</sub>
AMF <sub>LNO<sub>x</sub></sub>	S <sub>NO<sub>2</sub></sub>	V <sub>LNO<sub>x</sub></sub>
AMF <sub>NO<sub>x</sub>Vis</sub>	S <sub>NO<sub>2</sub></sub>	V <sub>NO<sub>x</sub>Vis</sub>

<sup>1</sup>The part of simulated VCD seen by OMI <sup>2</sup>The simulated VCD

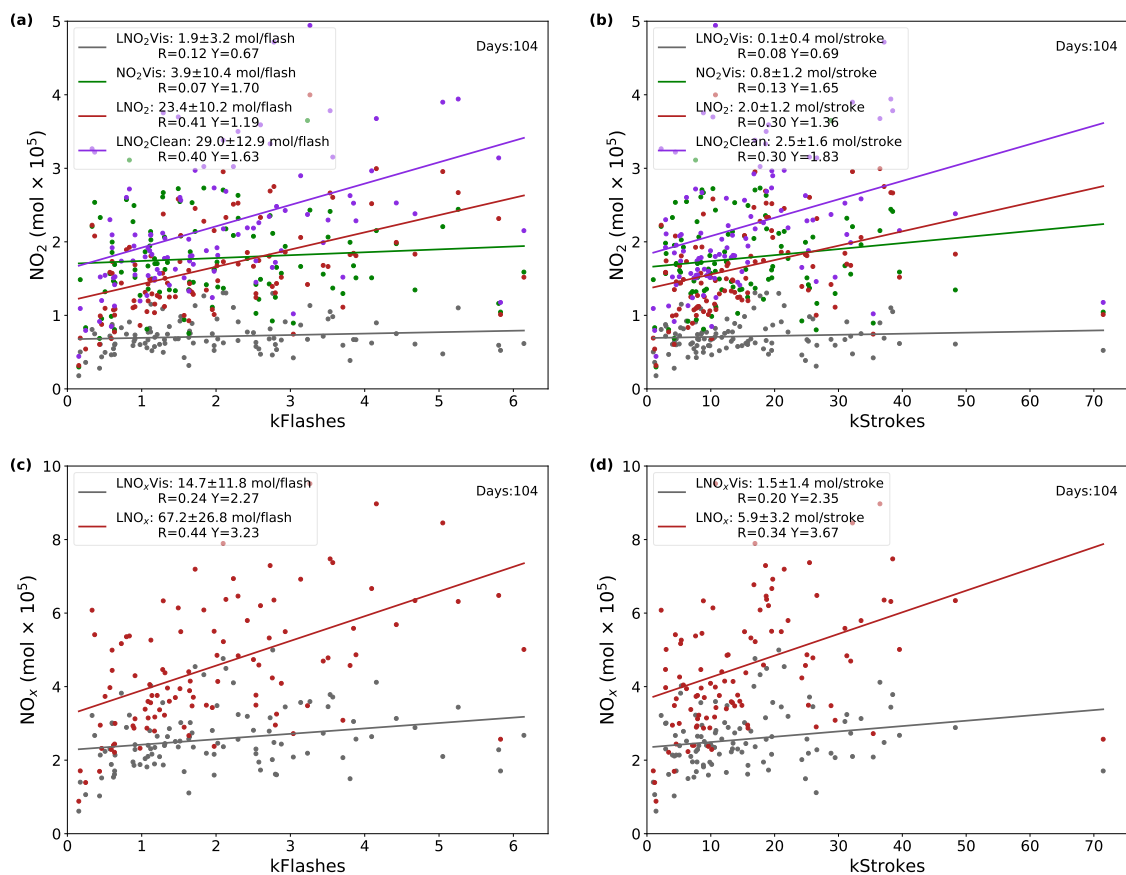


**Figure B1.** Linear regressions with  $\text{CRF} \geq 90\%$  and a flash threshold of  $1 \text{ flash box}^{-1}$  or  $3.4 \text{ strokes box}^{-1}$  per 2.4 h. (a) Daily  $\text{NO}_2$  Vis,  $\text{LNO}_2$  Vis,  $\text{LNO}_2$  and  $\text{LNO}_2$ Clean versus ENTLN total flashes data. (b) Same as (a) but for strokes. (c) Daily  $\text{LNO}_x$  Vis and  $\text{LNO}_x$  versus total flashes. (d) Same as (c) but for strokes.

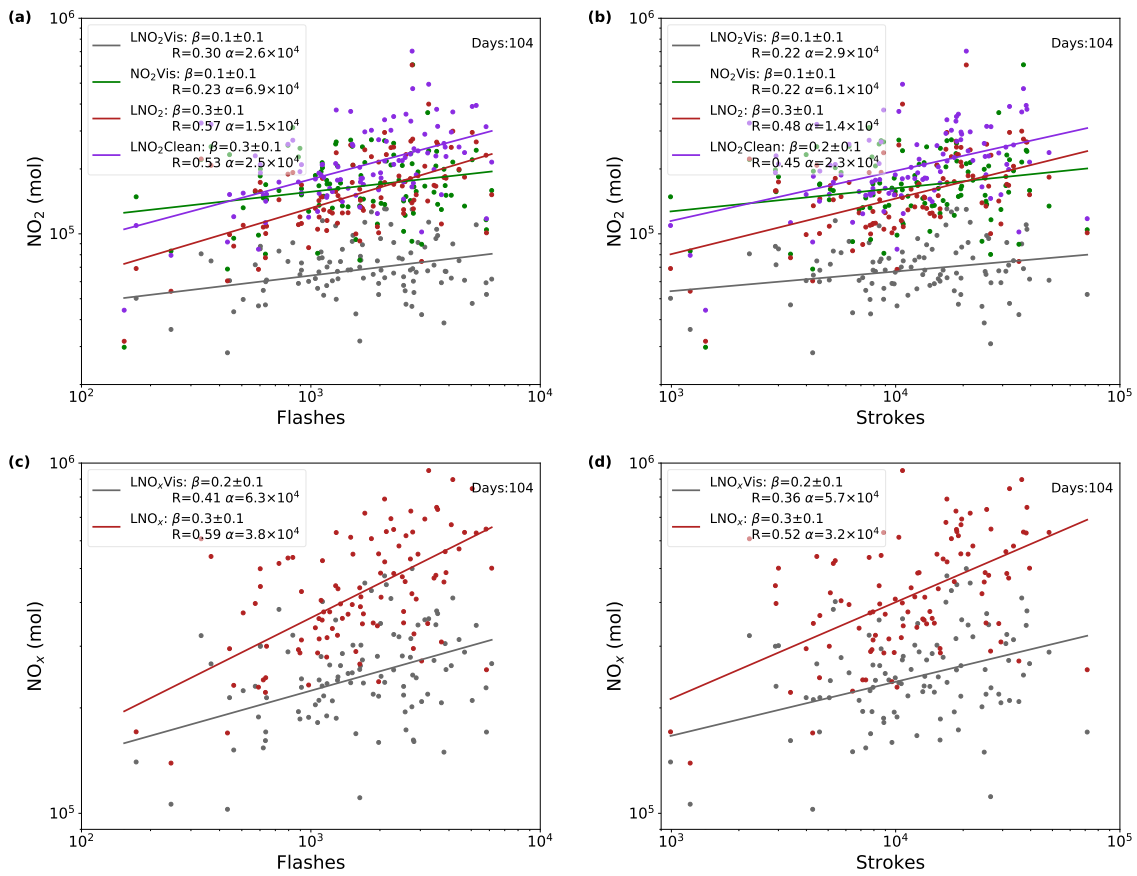


**Figure B2.** Same as Fig. B1 but using log-log axes.

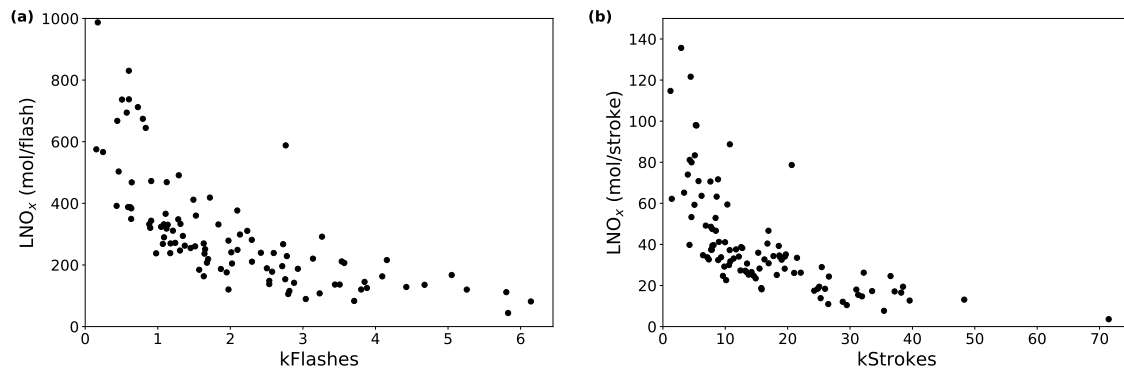


**Figure B3.** (a) Daily LNO<sub>x</sub> production efficiencies versus ENTLN total flashes data, with CRF  $\geq 90\%$  and a flash threshold of 1 flash box<sup>-1</sup>. (b) Same as (a) but for strokes.